Effects of Nonequilibrium Atmospheric-Pressure O_2 Plasma-Assisted Annealing on Anatase TiO_2 Nanoparticles

Retsuo Kawakami[*,1], Yuki Yoshitani[1], Akihiro Shirai[1], Shin-ichiro Yanagiya[1], Hirofumi Koide[1], Yuki Mimoto[1], Kosuke Kajikawa[2], Masahito Niibe[3], Yoshitaka Nakano[4], Chisato Azuma[1], and Takashi Mukai[5]

[1] *Graduate School of Technology, Industrial and Social Sciences, Tokushima University, Tokushima 770-8506, Japan*

[2]*Department of Biological Science and Technology, Faculty of Engineering, Tokushima University, Tokushima 770-8506, Japan*

[3] *Laboratory of Advanced Science and Technology for Industry, University of Hyogo, Kamigori, Hyogo 678-1205, Japan*

[4] *Chubu University, Kasugai, Aichi 487-8501, Japan*

[5] *Nichia Corporation, Anan, Tokushima 774-0044, Japan*

* Corresponding author. E-mail: retsuo@ee.tokushima-u.ac.jp, Phone: +81 88 656 7441, Fax: +81 88 656 7441

Abstract

Anatase TiO_2 nanoparticles (NPs) immobilized on glass substrates were annealed with the assistance of nonequilibrium atmospheric-pressure O_2 plasma. The plasma-assisted annealing greatly enhanced the photodecomposition and photobactericidal activity as compared with electric-furnace annealing. The plasma-assisted annealing reduced the TiO_2 NP agglomerate size and increased the optical absorption, the photoinduced electrical conductivity, the amounts of bridging and terminal oxygen groups, and the (112)/(101) plane intensity ratio, causing the lattice oxygen deficiency that formed partially Ti-rich surface portions. The enhanced photobactericidal activity would arise from the bridging and terminal oxygen groups. The enhanced photodecomposition would arise from the increased concentration of photogenerated carriers due to the following three factors. The first is the optical absorption increased by the agglomerate size reduction and the (112) plane growth or appearance, which exert scattering more incident photons. The second is the charge separation of photogenerated carriers facilitated by the bridging and terminal oxygen groups, which originate from oxygen vacancies via oxygen ion impact from the plasma. The third is the charge transfer of plasmon-excited electrons from the partially Ti-rich portions to TiO_2. The enhanced photodecomposition would also arise from more reactive oxygen species generated from the bridging and terminal oxygen groups by the photogenerated carriers.

Keywords: plasma-assisted annealing, anatase TiO_2 nanoparticles, photobactericidal activity, photodecomposition, bridging and terminal oxygen groups

1. Introduction

TiO_2 semiconductor photocatalysts are highly expected to be used as sterilization materials [1−5] and environmental purification materials [6−10]. This reason is that TiO_2 semiconductor photocatalysts have the strong oxidizing power, the chemical inertness, the non-toxicity, and the low-cost [11]. Reactive oxygen species (ROS) with high oxidizability are generated by photogenerated carriers in the TiO_2 surface irradiated with ultraviolet (UV) photons at higher energies than the bandgap energy of 3.0−3.2 eV. Since the generated ROS and/or photogenerated carriers play a crucial role on removing pollutants and bacteria, the photocatalytic process of TiO_2 semiconductors will not produce new pollutants and will not be accompanied with toxicity. In particular, the photocatalytic activity of anatase TiO_2 with a bandgap energy of 3.2 eV is higher than that of rutile TiO_2 with a bandgap energy of 3.0 eV, because anatase TiO_2 has a higher density of localized states that provide the charge separation in the form of trapping sites for photogenerated carriers [12]. The form of TiO_2 nanoparticles (NPs) also has a higher photocatalytic activity than the form of TiO_2 bulk does because of a larger effective surface-to-volume ratio [13−15]. In addition, post-annealing processes for 1 h in air at 400−600 °C increase the photocatalytic activity of TiO_2 owing to the crystallinity improvement accompanied with forming larger crystallite sizes [16,17]. Thus, anatase TiO_2 NPs subjected to the post-annealing process are considered to have a much higher photocatalytic activity under UV irradiation.

Recently, we proposed a new post-treatment method, i.e., nonequilibrium atmospheric-pressure (NAP) O_2 plasma-assisted annealing, in order to enhance the photocatalytic activity of sputter-grown bronze TiO_2 thin films [18]. This method is characterized by the fact that the sample surface is less susceptible to plasma-induced damage because of lower energies of ions impinging from NAP plasma onto the surface [19] and because of damage recovery effects induced by annealing as in the case of GaN

[20]. The proposed plasma-assisted annealing greatly enhanced the photocatalytic activity of bronze TiO_2 thin films, grown without heating the glass substrate by using direct current facing-target sputtering (DC FTS) [18]. The photocatalytic activity of plasma-assisted-annealed bronze TiO_2 thin films was more enhanced than those of O_2 gas-annealed samples and NAP O_2 plasma-only-treated samples. The enhanced photocatalytic activity was comparable to that of commercial anatase TiO_2 NPs. This enhancement of photocatalytic activity was found to be attributed primarily to a crystalline transition from the bronze-phase to the anatase-phase, which exerted increasing the optical absorbance, and thus enhancing the concentration of photogenerated carriers [18]. However, we did not clarify whether the proposed plasma-assisted annealing further enhance the photocatalytic activity of TiO_2 NPs originally having an anatase-phase. This is strongly required to clarify the effectiveness of plasma-assisted annealing as a post-annealing process of anatase TiO_2 NPs.

In the present study, we investigate the effect of NAP O_2 plasma-assisted annealing on photocatalytic characteristics of anatase TiO_2 NPs immobilized on glass substrate, by employing a dielectric barrier discharge (DBD) plasma reactor equipped with a heater [18]. For comparison, anatase TiO_2 NPs immobilized on glass substrate were annealed at a variety of temperatures in ambient air by employing an electric furnace (EF). This EF annealing is well-known as a post-annealing process to enhance the photocatalytic activity, as described above. Regarding the photocatalytic activity evaluation, photodecomposition of methylene blue (MB) dye in solution and photoinactivation of *Bacillus subtilis* American Type Culture Collection (*B. subtilis* ATCC) 6633 [21] were performed under 3.4 eV photon irradiation (under 365-nm UV irradiation). The bactericidal assay was also performed without 3.4 eV photon irradiation. The conductivities of the samples in the presence and absence of 3.4 eV photon irradiation were measured in order to qualitatively compare the concentrations of photogenerated

carriers in the samples. The samples after the plasma-assisted annealing were analyzed by using X-ray diffraction (XRD) and X-ray photoelectron spectroscopy (XPS) in order to clarify the crystallization behavior and a chemical composition change at the surface, respectively. We characterize the plasma-assisted annealing effect by elucidating the differing characteristics of anatase TiO_2 NPs annealed with the assistance of NAP plasma and those annealed with EF. The present study is not only important to deeply understand the enhancement mechanism of anatase TiO_2 NPs photocatalytic activity induced by plasma-assisted annealing, but also indispensable for the practical fabrication of anatase TiO_2 NPs with excellent photocatalytic activity.

2. Experimental procedure

The samples used were anatase TiO_2 NPs with an averaged size of 7 nm (Ishihara Sangyo ST-01, Japan) immobilized on glass substrates 12.5 × 12.5 mm^2 in area, as shown in Fig. 1. The immobilization of anatase TiO_2 NPs can improve the sample handling. Prior to anatase TiO_2 NPs immobilization, the glass surfaces were treated for 10 min with a capacitively-coupled radio frequency (RF) argon plasma called a nonequilibrium low pressure argon plasma [22] in order to enhance the wettability of the glass substrate surfaces. The argon plasma was generated by a 13.56 MHz sinusoidal wave generator with a maximum voltage of 200 V at a low gas pressure of 60 Pa. The gas used was 99.999 vol% purity argon supplied at a gas flow rate of 15 ml/min from a high-pressure gas cylinder. The applied RF power was 60 W and the self-bias DC voltage generated at the sample stage was −200 V. After the argon plasma treatment, anatase TiO_2 NPs solution diluted with deionised water was dropped on the glass surface and naturally dried for 24 h at room temperature. The concentration and volume of dropped solution were 2.5×10^3 mass ppm and 100 μl, respectively. The thickness of immobilized anatase TiO_2 NPs was estimated to be approximately 400 nm from the mass density of anatase TiO_2, 3.89 g/cm^3

[23]. The immobilized TiO_2 NPs were not destroyed when immersed in an aqueous solution as shown in Fig. 1(b). However, in the case that the glass substrate surfaces were treated for less than 10 min with the argon plasma, the destruction of prepared samples was caused by immersing the samples in aqueous solution as shown in Fig. 1(c).

The samples were treated for 1 h with NAP plasma-assisted annealing in O_2 gas in a heater-equipped DBD plasma reactor [18]. The reactor was composed of a powered electrode plate and an electrically grounded electrode plate, each 40 mm in diameter, as shown in Fig. 2(a). The electrically grounded electrode plate was a sample stage connected to a heater controller, which maintained the temperature at 300 ℃. The powered electrode plate was covered with a 1-mm-thick alumina dielectric 50 mm in diameter, which prevented the onset of arc discharges characterized by high current densities [18]. NAP O_2 plasma was generated in a gap spacing of 2 mm at a gas pressure of 100 kPa with a 25 kHz sinusoidal wave generator. The gas used was 99.9 vol% purity O_2 supplied at a gas flow rate of 15 ml/min from a high-pressure gas cylinder. The waveforms of the applied voltage and discharge current are shown in Fig. 2(b). The discharge current led the applied voltage by 65 degrees. The current waveform is seen to be a roughly sinusoidal waveform mixed with a pulse per half cycle. This indicates that the plasma discharge with the external heating belongs to the glow-like discharge [24]. The root mean square (RMS) value of applied voltage was 900 V, and the RMS value of discharge current was 20 mA. The power consumption was 8 W, which was assessed by integrating the product of voltage and current waveforms over a single cycle. The spectrum of light emitted from NAP O_2 plasma with external heating has a peak at a wavelength of 777 nm, as in the case of capacitively-coupled RF O_2 plasmas at 1.3 to 13 Pa [25]. This emission spectrum was acquired with an exposure time of 3 s by using a spectrometer (Ocean optics USB4000). The observed peak corresponds to the emission of excited oxygen radicals, OI ($3p\,^5p \rightarrow 3s\,^5S$) [26]. These oxygen radicals are generated

predominantly through a dissociative process of O_2 via impact of energetic electrons, e + $O_2 \rightarrow O + O + e$ [27]. For comparison, the samples were annealed for 1 h at 300, 400 and 500 ℃ in air by using an EF (Nitto Kagaku NHK-120BS-II, Japan). The sample surfaces after each annealing treatment were irradiated for 2 h with 3.4 eV photons in order to remove organic impurities. The UV source was a light-emitting diode (LED, Nichia NVSU333A, Japan). The UV intensity at the sample surface was 100 mW/cm^2. The flux of UV photons impinging on the surface was estimated to be 1.8×10^{17} cm^{-2}s^{-1}.

For evaluating the photocatalytic activity, we performed the MB dye photodecomposition experiment under 3.4 eV photon irradiation. The concentration and volume of MB dye solution were 10 mass ppm and 4 ml, respectively. The UV source and UV intensity were the same as those used for removing contamination on the surface, respectively. Prior to UV irradiation, the samples were dipped in the MB solution for 1 h under a dark condition in order to ensure that the adsorption reached the equilibrium. Afterwards, the dipped samples were irradiated for 1 and 2 h with UV photons. The photodecomposition value of MB dye concentration, $|\ln(C/C_0)|$ [28,29], was determined by using a spectrophotometer (Otsuka Electronics Photal MCPD-370A, Japan). The symbols C_0 and C were the MB dye concentrations before and after UV irradiation, respectively.

We also performed the photoinactivation of *B. subtilis* ATCC 6633 [21] in the following process. The strain was grown for 17 h in Luria-Bertani (LB) broth (Nacalai Tesque Lennox, Japan) at 37 ℃ under shaking at 160 rpm. In order to remove the broth, the grown suspension was cooled at 4 ℃, centrifuged at 6570 *g* for 3 min, where *g* is the centrifugal acceleration, and washed twice with 0.8% NaCl solution (saline solution). Afterwards, the bacterial suspension with 2×10^7 colony-forming unit per ml (CFU/ml) was prepared in sterile ion-exchanged water. Immediately after the bacterial suspension (0.01 ml) was dropped on the sample surface, the dropped surface was irradiated for 30 s

with 3.4 eV photons emitted from a LED (Nichia NVSU233A, Japan). The UV intensity at the surface was 63.3 mW/cm^2, and the flux of photons impinging on the surface was 1.2×10^{17} cm^{-2}s^{-1}. In order to extract the bacteria from the sample, the sample after the UV irradiation was homogenized in 10 ml solution of soybean-casein digest lecithin polysorbate (SCDLP, Nihon Pharmaceutica, Japan) broth for 1 min. Aliquate of the broth suspension containing bacteria (0.1 ml) was subjected to 10-fold serial dilutions with SCDLP broth. Each serial dilution was plated on SCDLP agar plates and incubated for 48 h at 37 ℃ in an incubator. After 48 h, the log number of viable cells was measured by using colony counting method [30,31]. Specifically, the log survival count was estimated from the equation, log N, where N is the number of CFU after 48-h dark incubation following UV irradiation [32,33]. We performed the photobactericidal assay three times and averaged the measured data. The bactericidal effects of samples in the absence of UV irradiation were also investigated in order to clarify the net photocatalytic effect.

The crystalline structures of treated samples were measured by using in-plane mode of XRD (Rigaku SmartLab, Japan). The X-ray source was Cu Kα radiation (8040 eV). The chemical compositions of treated sample surfaces were measured by using XPS (Ulvac-Phi PHI500, Japan). Ti 2p and O 1s peaks were measured from the treated sample surfaces under Al Kα radiation (1486.6 eV). The UV absorption coefficients of treated samples were measured by using UV-visible absorption spectroscopy (Hitachi U-3900, Japan). In particular, we analyzed the absorption coefficients at a photon energy of 3.4 eV. The electrical conductivities parallel or horizontal to the sample surface were measured by using electrical impedance spectroscopy (Hioki 3522 LCR HiTESTER, Japan). These electrical conductivities were estimated from subtracting the electrical resistance of glass substrate. We comparatively analyzed the conductivities in the presence and absence of 3.4 eV photon irradiation with a flux of 1.8×10^{17} cm^{-2}s^{-1}.

3. Results

3.1. Photocatalytic characteristics

Figure 3(a) shows the comparison between the MB dye photodecomposition values, $|\ln(C/C_0)|$, of untreated TiO_2 NPs and plasma-assisted-annealed TiO_2 NPs. Here, it should be noticed that a large value of $|\ln(C/C_0)|$ signifies a high photodecomposition effect. The photodecomposition value of untreated TiO_2 NPs increases from 0 to 0.7 as the UV irradiation time lengthens from 0 to 2 h. The photodecomposition of plasma-assisted-annealed TiO_2 NPs greatly increases as compared with untreated TiO_2 NPs. Specifically, the photodecomposition value of plasma-assisted-annealed TiO_2 NPs at an UV irradiation time of 2 h, 1.4, is approximately two times higher than that of untreated TiO_2 NPs. This comparison indicates that the plasma-assisted annealing enhances the photodecomposition of anatase TiO_2 NPs, as in the case of sputter-grown bronze TiO_2 thin film [18]. Figure 3(b) shows the photodecomposition values of TiO_2 NPs annealed at a variety of temperatures in the EF. The photodecomposition increases as the EF-annealing temperature rises to 400 ℃. Specifically, at an UV irradiation time of 2 h, the photodecomposition value of TiO_2 NPs annealed at 400 ℃, 0.9, is approximately 1.4 times higher than that of untreated TiO_2 NPs. With a further rise in the EF annealing temperature to 500 ℃, the photodecomposition greatly decreases as compared with that of untreated TiO_2 NPs. This decrease can be attributed to a crystalline transition from the anatase phase to the rutile phase, as discussed in the literature [12,34]. Thus, the comparison between Figs. 3(a) and 3(b) indicates that the plasma-assisted annealing is more effective than the EF annealing for enhancing the photodecomposition of anatase TiO_2 NPs.

The bactericidal efficacy of untreated, plasma-assisted-annealed, and 400 ℃ EF-annealed samples in the presence and absence of UV irradiation are compared as shown in Fig. 4. The result of glass without TiO_2 NPs is also described in the same figure in

order to deepen the understanding of photobactericidal efficacy. Here, it should be noticed that a small log survival count signifies a high bactericidal activity. The log survival count of glass in the presence of UV irradiation, 6, is smaller than or comparable to that of glass in the absence of UV irradiation, 5.9. This suggests that the photobactericidal activity hardly occurs owing to 3.4 eV photon irradiation for 30 s in the case that TiO_2 NPs are not used. In the absence of UV irradiation, the log survival count of plasma-assisted-annealed TiO_2 NPs, 2.5, is the smallest among the samples. The survival counts of EF-annealed TiO_2 NPs and untreated TiO_2 NPs are similar each other, and their values are roughly comparable to that of glass. In the presence of UV irradiation, the log survival count of plasma-assisted-annealed TiO_2 NPs, 2.0, is also the smallest among the samples. However, there is no significant difference between the log survival counts of this sample in the presence and absence of UV irradiation. Specifically, the plasma-assisted-annealed TiO_2 NPs reduce the survival number by four orders of magnitude, regardless of UV irradiation. Thus, the plasma-assisted annealing is found to be more effective for enhancing the photobactericidal activity of anatase TiO_2 NPs.

3.2. Crystalline structure

Figure 5 shows the comparison between XRD patterns of untreated, plasma-assisted-annealed, and EF-annealed TiO_2 NPs. The XRD patterns are superimposed on a halo pattern of the glass substrate. The XRD pattern of untreated TiO_2 NPs is composed of (101), (112), (200), and (105) plane orientations of anatase crystalline structure with lattice parameters, $a = b = 3.79$ Å and $c = 9.51$ Å [35]. The intensity of (101) diffraction peak is much larger than those of other diffraction peaks. This XRD result is consistent with those reported in the literature of anatase TiO_2 NPs, ST-01 [36,37]. The XRD pattern of plasma-assisted-annealed TiO_2 NPs is fundamentally similar to that of untreated TiO_2 NPs. However, the integrated intensities of the diffraction peaks from the samples are

seen to differ from each other when compared in detail. A similar result is observed for EF-annealed TiO_2 NPs; the XRD pattern of treated sample does not significantly change from that of the untreated sample. Thus, the plasma-assisted annealing of anatase TiO_2 NPs neither causes the crystalline transition nor changes the plane orientations, as in the case of EF annealing. This differs from the result of bronze TiO_2 thin films grown by DC FTS, which causes the crystalline transition [18].

3.3. Chemical compositions

Figure 6 shows the comparison between Ti 2p regions of measured XPS spectra of untreated, plasma-assisted-annealed, and EF-annealed TiO_2 NPs. Each of the spectra has Ti $2p_{3/2}$ and Ti $2p_{1/2}$ peaks at 457.8 and 463.5 eV due to Ti−O bond, respectively [38−40]. The spectrum of plasma-assisted-annealed TiO_2 NPs is the same as those of untreated and EF-annealed TiO_2 NPs. This suggests that the plasma-assisted annealing does not influence the Ti 2p peak as in the case of EF annealing. In contrast, the measured O 1s spectrum of plasma-assisted-annealed TiO_2 NPs significantly differs from those of untreated and EF-annealed TiO_2 NPs. Figure 7 shows the comparison between O 1s regions of measured XPS spectra of untreated, plasma-assisted-annealed, and EF-annealed TiO_2 NPs (red open circles). The plasma-assisted annealing increases the peak intensity at a binding energy of 532 eV in the O 1s spectrum. A clear difference between the O 1s spectra of the samples is quantitatively established by decomposing the spectra into three pseudo-Voigt functions shown in Fig. 7 (purple, green, and blue curves). The pseudo-Voigt functions located at 529.7, 531.0, and 532.3 eV are associated with O−Ti bond in TiO_2 lattice, bridging oxygen groups, and basic terminal oxygen groups adsorbed on the surface, respectively [41,42]. The curves formed by summing the three pseudo-Voigt functions correspond to the black curves that reproduce the measured spectra.

The peak decomposition analysis reveals the effect of plasma-assisted-annealing as

shown in Fig. 8. Figures 8(a)−8(c) show the O/Ti ratios of O−Ti bond, bridging oxygen groups, and terminal oxygen groups for the three samples, respectively. The O/Ti ratio of O−Ti bond is calculated by multiplying the total O/Ti ratio by its fraction estimated from the peak decomposition. The total O/Ti ratio is defined by the ratio of integrated intensity of measured O 1s peak to integrated intensity of measured Ti 2p peak. The O/Ti ratios of bridging and terminal oxygen groups are acquired as in the case of the O/Ti ratio of O−Ti bond. The O/Ti ratio of O−Ti bond for untreated TiO_2 NPs, 1.9, is roughly equivalent to that estimated from the stoichiometry of TiO_2. However, the O/Ti ratios of bridging and terminal oxygen groups for this sample are seen to be non-zero; their values are estimated to be 0.2 and 0.7, respectively. This comparison suggests that, in the case of untreated TiO_2 NPs, the total amount of bridging and terminal oxygen groups on the surface due to exposure to air is approximately half that of lattice oxygen atoms in O−Ti−O linkages. The plasma-assisted annealing decreases the O/Ti ratio of O−Ti bond. This reduction is also observed in EF annealing. In contrast, the plasma-assisted annealing increases the O/Ti ratio of bridging oxygen groups. The plasma-assisted annealing also increases the O/Ti ratio of terminal oxygen groups. The EF annealing hardly influences the O/Ti ratios of bridging and terminal oxygen groups. Thus, the plasma-assisted annealing causes the lattice oxygen deficiency and increases the amounts of bridging and adsorbed oxygen groups, whereas the EF annealing only causes the lattice oxygen deficiency, not influencing the amounts of bridging and adsorbed oxygen groups.

3.4. UV absorption

The UV absorption coefficients of plasma-assisted-annealed and EF-annealed samples significantly differ from each other, as shown in Fig. 9. These two annealing processes increase the absorption coefficient of untreated TiO_2 NPs. In particular, the plasma-assisted annealing greatly increases the absorption coefficient as compared with

EF annealing. The absorption coefficient of plasma-assisted-annealed TiO_2 NPs is 1.5 times higher than that of EF-annealed TiO_2 NPs. This difference suggests that the plasma-assisted-annealed TiO_2 NPs absorb 1.5 times higher number of 3.4 eV photons. The difference also suggests that the penetration depth of 3.4 eV photons is shallower in the case of plasma-assisted annealing, because the UV penetration depth is inversely proportional to the optical absorption coefficient [43]. Thus, the plasma-assisted annealing of TiO_2 NPs enhances the absorption of 3.4 eV photons near the outermost surface, in comparison with the EF annealing.

3.5. Electrical conductivity

We compare the conductivities of the samples in the presence and absence of 3.4 eV photon irradiation, as shown in Fig. 10(a). In the absence of UV photon irradiation, the conductivity of plasma-assisted-annealed TiO_2 NPs is much lower than that of untreated TiO_2 NPs. This conductivity is also low compared with EF annealing. This suggests that the plasma-assisted annealing greatly reduces the concentration of residual charged carriers as compared with EF annealing. The residual charged carriers are attributed to oxygen vacancies unintentionally introduced in TiO_2, which act as shallow donors located at 0.75−1.18 eV below the conduction band edge [44,45]. The UV photon irradiation increases the conductivity of each sample, which comes from the generation of photogenerated carriers. The UV-induced relative conductivities defined by a difference between the conductivities with and without UV irradiation are comprehensibly compared as shown in Fig. 10(b). The UV-induced relative conductivity of plasma-assisted-annealed TiO_2 NPs is large compared with those of EF-annealed TiO_2 NPs and untreated TiO_2 NPs. This indicates that the plasma-assisted annealing greatly enhances the concentration of photogenerated carries as compared with EF annealing.

4. Discussion

The enhanced photodecomposition of TiO_2 NPs due to the plasma-assisted annealing correlate closely with the increased UV-induced relative conductivity (Fig. 10(b)). This correlation clearly indicates that the plasma-assisted-annealing increases the concentration of photogenerated carriers. The photodecomposition of MB in water is known to be attributed predominantly to ·OH radicals generated in TiO_2 irradiated with UV [46,47]. These radicals are generated by oxidation of H_2O due to photogenerated holes h^+ [46],

$$H_2O + h^+ \rightarrow H^+ + \cdot OH \quad (1)$$

and by transient formation of hydroperoxide radicals driven via reduction of O_2 due to photogenerated electrons e^- [46],

$$O_2 + e^- \rightarrow \cdot O_2^- \quad (2)$$

$$O_2^- + H^+ \rightarrow \cdot O_2H \quad (3)$$

$$2 \cdot O_2H \rightarrow H_2O_2 + O_2 \quad (4)$$

$$H_2O_2 + e^- \rightarrow OH^- + \cdot OH \quad (5)$$

Thus, more ·OH radicals are considered to be generated in the plasma-assisted annealing because of the increased photogenerated carrier concentration. This would contribute to the enhanced photodecomposition. However, the increased concentration of photogenerated carries cannot be explained in terms of the crystalline transition that increases the optical absorption, as in the case of TiO_2 thin films grown by DC FTS [18]. This is because, in the case of anatase TiO_2 NPs, there is no crystalline transition due to the plasma-assisted annealing (Fig. 5).

From other points of view, there are three possible factors for explaining the increased concentration of photogenerated carries. The first factor is the increased optical absorption (Fig. 9), which can originate from the size reduction of TiO_2 NP agglomerates induced by plasma-assisted annealing (Fig. 11). Figure 11 shows the surface

morphologies of the samples, which were observed by scanning electron microscopy (SEM, JEOL JSM-6390). Each sample surface is composed of a large number of TiO_2 NP agglomerates or TiO_2 NPs-agglutinated grains. In particular, the number of the agglomerates with large sizes more than 50 μm is seen to be smaller in the case of plasma-assisted annealing as shown in Table I. In contrast, the number of the agglomerates with small sizes less than 20 μm is seen to be larger for the plasma-assisted annealing. This suggests that the plasma-assisted annealing reduces the agglomerate size. This is also confirmed from the RMS surface roughness acquired with a scanning area of 100 × 100 μm^2 by using atomic force microscope (Hitachi High-Technologies AFM5500M, Japan). The RMS surface roughness of plasma-assisted-annealed sample is 0.15 μm, which is smaller than that of the untreated sample, 1.2 μm, and that of EF-annealed sample, 0.50 μm. This comparison suggests the size reduction of the agglomerate in the case of the plasma-assisted-annealing. This size reduction scatters more incident UV photons, which can contribute to the increased optical absorption and thus increases the concentration of photogenerated carriers. Moreover, the increased optical absorption can also originate from the growth or appearance of anatase (112) plane orientation facilitated by the plasma-assisted annealing. Figure 12 shows the (112)/(101) plane intensity ratios estimated from the integrated intensity ratios of (112) to (101) diffraction peaks shown in Fig. 5. The photocatalytic activity of anatase (112) plane-orientated TiO_2 surface is reported to be approximately two times higher than that of anatase (101) plane-orientated TiO_2 surface [48,49]. This higher photocatalytic activity stems from the fundamental fact that the morphologies of (101) plane- and (112) plane-orientated surfaces differ from each other [50−52]. The morphology of (101) plane-orientated surface is characterized by a terrace-like structure [50]. In contrast, the morphology of (112) plane-orientated surface is characterized by a zig-zag structure with a ridge and a groove, which contributes to scattering more incident UV photons, increases the optical absorption, and thus bringing

about a higher photocatalytic activity [48−52]. As shown in Fig. 12, the (112)/(101) plane intensity ratio of plasma-assisted-annealed TiO_2 NPs is higher than that of untreated TiO_2 NPs and that of EF-annealed TiO_2 NPs. This suggests that the plasma-assisted annealing causes the growth or appearance of (112) plane orientation. Thus, the plasma-assisted annealing facilitates the size reduction of TiO_2 NP agglomerates and the growth or appearance of (112) plane orientation, exerts scattering more incident UV photons, and increases the optical absorption. This would contribute to enhancing the photogenerated carrier concentration.

The second factor for enhancing the photogenerated carrier concentration is the facilitated charge separation of photogenerated carriers [53,54] due to the increased amounts of bridging and terminal oxygen groups (Figs. 7 and 8), which originate from oxygen vacancies generated via impact of oxygen ions from NAP O_2 plasma. Figure 13 shows the fluences of oxygen-based species impinging from NAP O_2 plasma onto the surface, which are simulated by coupling plasma hybrid module (PHM) [55] and neutral momentum equation module (NMEM) [56] supplied by PEGASUS software Inc., Japan. This simulation is performed under the same condition as in the experiment, by taking into account the DBD plasma reactor geometry. PHM simulates the motions of charged particles in gases under electric field by solving plasma fluid equations [57,58]. NMEM simulates the motion of neutral particles by solving the Navier-Stokes equation [59,60]. The simulated result suggests that oxygen radicals from the plasma can stick on the surface, which agrees with the presence of oxygen radicals observed in the emission spectrum of NAP O_2 plasma. This agreement assures the validity of the simulation model. The simulated result also suggests that O_2^+, O_2^-, and O_3^- oxygen ions coming from the plasma can impinge on the surface. The simulated average energies of oxygen ions are lower than 1 eV, which is consistent with literature [61]. O_2^+ ions are generated through an ionization process, $e + O_2 \rightarrow O_2^+ + 2e$ [27]. O_2^- ions are generated mainly through a

dissociative attachment process, $e + O_3 \rightarrow O_2^- + O$, where the generation of O_3 is due to a detachment process of $O^- + O_2 \rightarrow O_3 + e$ and the generation of O^- is due to a dissociative attachment process, $e + O_2 \rightarrow O^- + O$ [27]. O_3^- ions are generated through charge transfer processes, $O^- + O_3 \rightarrow O_3^- + O$ and $O_2^- + O_3 \rightarrow O_3^- + O_2$ [27]. The impact of oxygen ions from the plasma on the TiO_2 surface can create oxygen vacancies in the surface as reported in literature [62,63] and as shown in Fig. 14. Figure 14 shows the depth profiles of oxygen vacancies created in TiO_2 NPs via the impact of the oxygen ions shown in Fig. 13, which are calculated from simulation of atomic scattering in amorphous material based on liquid model (SASAMAL) [64] supplied by PEGASUS software Inc., Japan. SASAMAL calculates the motion of particles in amorphous solid by using the same binary collisional approximation method as that used for simulating transport of ions in amorphous matter, called as TRIM [65]. The calculated result suggests that the created oxygen vacancies are distributed in the region from the surface to a depth of approximately 2 nm. The created oxygen vacancies on the surface play an important role in adsorbing more oxygen molecules and radicals [62,63,66,67]. Oxygen molecules and oxygen radicals from the plasma are preferentially adsorbed on the subsurface oxygen vacancies with negative charges, and capture or share the excess electrons located on the oxygen vacancy state [62,63,66,67]. In other words, more oxygen molecules and oxygen radicals are adsorbed in the presence of the oxygen vacancies, decreasing the concentration of residual charged carriers in the TiO_2 surface (decreasing the electrical conductivity of the sample). This agrees with the observed data: the increased amounts of bridging and terminal oxygen groups (Figs. 7 and 8) and the decreased electrical conductivity due to plasma-assisted annealing (Fig. 10(a)). The decrease in the residual charged carrier concentration increases the depletion layer width from the surface because the depletion layer width increases in proportion to the reverse square of carrier concentration [68,69]. The increase in the depletion layer width extends the near-surface

electric field distribution strongly responsible for the charge separation of photogenerated carries [68,69]. This can facilitate the charge separation, reduce the carrier recombination, and prolong the carrier lifetime. The prolonged carrier lifetime contributes to an increase in the carrier concentration. Thus, the plasma-assisted annealing would facilitate the charge separation owing to the increased amounts of bridging and terminal oxygen groups originating from the plasma-induced oxygen vacancies, enhancing the photogenerated carrier concentration.

The third factor for increasing the photogenerated carrier concentration is the charge transfer effect of plasmon-excited electrons [70−72] from Ti to TiO_2. The impact of oxygen ions on the TiO_2 surface can preferentially remove lattice oxygen atoms from the surface [73,74]. The lattice oxygen atoms are also removed from the surface by sublimation or evaporation during recrystallization induced by conductive heating from the plasma and annealing [63,75]. This is confirmed by the lattice oxygen deficiency observed in Fig. 8(a). The removal of lattice oxygen atoms is considered to unintentionally cause partially Ti-rich surface portions, i.e., partial Ti nanoisland-like structures. This is roughly similar to metallic nanostructures decorated on metal oxides, for example, Au nanostructure-decorated TiO_2 and Ti nanostructure-decorated ZnO [70−72]. In the case of metallic nanostructures-decorated oxides, hot-electrons are generated by increasing the optical absorption through localized surface plasmon resonance (LSPR) in metallic nanostructures irradiated with photons (plasmon-excited electrons occur), transferring from the metal nanostructures to the oxides [70−72]. This accordingly increases the concentration of photogenerated carriers in the oxides. From the structural similarity, we suggest that there is the LSPR effect induced from the partially Ti-rich surface portions as in the case of metallic nanostructures-decorated oxides. This is supported by the observed data demonstrating the increased optical absorption (Fig. 9). Thus, plasmon-excited electrons transferring from the partially Ti-

rich surface portions to TiO_2 would contribute to enhancing the photogenerated carrier concentration. Even in the EF annealing, the charge transfer effect of plasmon-excited electrons would also occur because of the lattice oxygen deficiency observed in Fig. 8(a). In order to further demonstrate the contribution of the charge transfer, electrochemical impedances across the samples (perpendicular to the sample surface) were measured by using electrochemical impedance spectroscopy (Solartron Analytical 1280C) as shown in Fig. 15. Figure 15 shows Nyquist plots of the samples, which include the data of the glass substrate. A small circular diameter signifies a low resistance of charge transfer [76]. The plasma-assisted-annealed and EF-annealed samples have similar diameters. These diameters are smaller than that of the untreated sample, indicating that the charge transfer is more likely to occur in these annealed samples. This can also support the contribution of the charge transfer.

The enhanced photodecomposition of TiO_2 NPs due to the plasma-assisted annealing would also be relevant to the increased amounts of bridging and terminal oxygen groups on the surface (Figs. 8(b) and 8(c)). These oxygen groups are easily activated by photogenerated carriers [77]. Photogenerated electrons can transfer to the bridging and terminal oxygen groups, generating superoxide anion radicals $\cdot O_2^-$ [77]. Photogenerated holes can oxidize the majority of $\cdot O_2^-$ into singlet oxygen $^1O_2$ [77]. In the case of plasma-assisted-annealed TiO_2 NPs, more photo-chemically-excited oxygen radials such as O_2^- and $^1O_2$ are considered to be generated because of both the increased amounts of bridging and terminal oxygen groups and the higher concentration of photogenerated carriers. These radicals contribute to the generation of more ·OH radicals through a series of chemical reactions of (2) to (5) described above. This would also be responsible for the enhanced photodecomposition.

Based on the above-discussed four key factors, the enhancement mechanism of photodecomposition induced by plasma-assisted annealing is summarized in Fig. 16.

Figure 16 shows the proposed band energy diagrams and structural models of plasma-assisted-annealed anatase TiO_2 surfaces for the four key factors. Firstly, the photogenerated carrier concentration is enhanced owing to the optical absorption increased by the size reduction of TiO_2 NP agglomerates and the growth or appearance of anatase (112) plane orientation (Fig. 16(a)). Secondary, the photogenerated carriers are effectively separated by increasing the depletion layer width owing to more bridging and terminal oxygen groups originating from the plasma-induced oxygen vacancies (Fig. 16(b)). Thirdly, the plasmon-excited electrons transferring from the partially Ti-rich surface portions to TiO_2 also contribute to enhancing the photogenerated carrier concentration (Fig. 16(c)). Fourthly, these photogenerated carriers generate more ROS from the bridging and terminal oxygen groups (Fig. 16(d)). These four key factors would synergistically boost the generation of more ·OH radicals, and thus enhancing the photodecomposition.

The plasma-assisted annealing greatly enhances the photobactericidal activity of anatase TiO_2 NPs as compared with EF annealing. This occurs even in the absence of UV irradiation (Fig. 4). This finding suggests the enhancement mechanism of photobactericidal activity significantly differs from that of MB photodecompositon that occurs only in the presence of UV irradiation. Specifically, the enhanced photobactericidal activity cannot be explained from the viewpoint of the above-discussed four key factors. The bactericidal activity in the absence of UV irradiation is considered to correlate closely with the amounts of bridging and terminal oxygen groups (Figs. 7 and 8). This correlation suggests that the enhanced photobactericidal activity is attributed predominantly to the increased amounts of bridging and terminal oxygen groups. These amounts may be greater than that of ROS normally generated by the photogenerated carriers. The direct contact of the bacteria with the increased amounts of bridging and terminal oxygen groups may induce bacterial membrane stress or oxidative stress, which

causes physical damage of bacterial membranes, loss of bacterial membrane integrity, and ribonucleic acid leakage [78−80]. This would contribute to destroying or inhibiting the microorganism growth and reproduction. For the detailed mechanism of the enhanced photobactericidal activity, the photoinactivation effect of Gram-positive and -negative bacteria [81,82] will need to be clarified in the future.

5. Conclusion

We have clarified the effect of NAP O_2 plasma-assisted annealing on the photocatalytic characteristics of anatase TiO_2 NPs, by comparing it with EF annealing effect. The plasma-assisted annealing greatly enhances the photodecomposition and photobactericidal activity of TiO_2 NPs as compared with EF annealing. The plasma-assisted annealing increases the optical absorption, the amounts of bridging and terminal oxygen groups, and the (112)/(101) plane intensity ratio without changing the anatase phase. In contrast, the plasma-assisted annealing reduces the size of TiO_2 NP agglomerates and the electrical conductivity but increases the UV-induced relative conductivity proportional to the concentration of photogenerated carriers. Moreover, the plasma-assisted annealing causes the lattice oxygen deficiency on the surface, forming the partially Ti-rich surface portions. The enhanced photobactericidal activity would be due to the large amounts of bridging and terminal oxygen groups, which may induce the bacteria membrane stress or the oxidative stress connected to destroying or inhibiting the microorganism growth and reproduction. The enhanced photodecomposition would be due to the increase in the effective concentration of photogenerated carriers attributed to the synergetic effect of the following three factors. The first factor is the optical absorption increased by the agglomerate size reduction and the growth or appearance of anatase (112) plane orientation, which exert scattering more incident UV photons. The second factor is the charge separation of photogenerated carriers facilitated by the large amounts

of bridging and terminal oxygen groups, which originate from the oxygen vacancies generated via the impact of oxygen ions from the plasma. The third factor is the charge transfer effect of plasmon-excited electrons from the partially Ti-rich surface portions to TiO_2. The enhanced photodecomposition would also be due to more ROS generated from the large amounts of bridging and terminal oxygen groups by the photogenerated carriers.

Acknowledgments

We thank President and CEO Toshihide Takasaki, Dr. Hiroshi Nakadate, and Dr. Fumihiko Matsunaga of PEGASUS Software Inc., Chuo-ku, Tokyo, Japan for providing simulation software.

References

[1] Y. H. Chai, F. Zhou, and Z. Zhu, High-efficiency and environment-friendly sterilization PEVE coatings modified with Bi_2WO_6/TiO_2 composites, Chem. Phys. Lett. **715** (2019) 173−180.

[2] H. Liu, X. Hou, T. Sun, J. Yao, P. Wu, D. Li, J. Li, and J. Han, Cytocompatibility and antibacterial property of N^+ ions implanted TiO_2 nanotubes, Surf. Coat. Tech. **359** (2019) 468−475.

[3] R. Sadowski, A. Wach, M. Buchalska, P. Kustrowski, and W. Macyk, Photosensitized TiO_2 films on polymers – Titania-polymer interactions and visible light induced photoactivity, Appl. Surf. Sci. **475** (2019) 710−719.

[4] N. Liu, Q. Zhu, N. Zhang, C. Zhang, N. Kawazoe, G. Chen, N. Negishi, and Y. Yang, Superior disinfection effect of Escherichia coli by hydrothermal synthesized TiO_2-based composite photocatalyst under LED, Environ. Pollut. **247** (2019) 847−856.

[5] Z. Zhu, F. Zhou, S. Zhan, Y. Tian, and Q. He, Study on the bactericidal performance of graphene/TiO_2 composite photocatalyst in the coating of PEVE, Appl. Surf. Sci. **430** (2018) 116−124.

[6] N. Negishi, M. Sugasawa, Y. Miyazaki, Y. Hirami, and S. Koura, Effect of dissolved silica on photocatalytic water purification with a TiO_2 ceramic catalyst, Water Res. **150** (2019) 40−46.

[7] N. Negishi, Y. Miyazaki, S. Kato, and Y. Yang, Effect of HCO_3^- concentration in groundwater on TiO_2 photocatalytic water purification, Appl. Catal. B Environ. **242** (2019) 449−459.

[8] B. G. T. Keerthana and P. Murugakoothan, Synthesis and characterization of CdS/TiO_2 nanocomposite: methylene blue adsorption and enhanced photocatalytic activities, Vacuum **159** (2019) 476−481.

[9] B. J. Cha, S. Saqlain, H. O. Seo, and Y. D. Kim, Hydrophilic surface modification of

TiO_2 to produce a highly sustainable photocatalyst for outdoor air purification, Appl. Surf. Sci. **479** (2019) 31−38.

[10] H. J. Kim, Y. S. Yoon, K. H. Yang, and S. J. Kwon, Durability and purification performance of concrete impregnated with silicate and sprayed with photocatalytic TiO_2, Constr. Build. Mater. **199** (2019) 106−114.

[11] C. Lai, M. M. Wang, G. M. Zeng, Y. G. Liu, D. L. Huang, C. Zhang, R. Z. Wang, P. Xu, M. Cheng, C. Huag, H. P. Wu, and L. Qin, Synthesis of surface molecular imprinted TiO_2/graphene photocatalyst and its highly efficient photocatalytic degradation of target pollutant under visible light irradiation, Appl. Surf. Sci. **390** (2016) 368−376.

[12] D. A. H. Hanaor and C. C. Sorrell, Review of the anatase to rutile phase transformation, J. Mater. Sci. **46** (2011) 855−874.

[13] Y. Z. C. Li, X. Liu, F. Gu, H. Jiang, W. Shao, L. Zhang, and Y. He, Synthesis and optical properties of TiO_2 nanoparticles, Mater. Lett. **61** (2007) 79−83.

[14] U. Nwankwo, R. Bucher, A. B. C. Ekwealor, S. Khamlich, M. Maaza, and F. I. Ezema, Synthesis and characterizations of rutile-TiO_2 nanoparticles derived from chitin for potential photocatalytic applications, Vacuum **161** (2019) 49−54.

[15] M. Guang, Y. Xia, D. Wang, X. F. Zeng, J. X. Wang, and J. F. Chen, Controllable synthesis of transparent dispersions of monodisperse anatase-TiO_2 nanoparticles and nanorods, Mater. Chem. Phys. **224** (2019) 100−106.

[16] I. Hadjoub, T. Touam, A. Chelouche, M. Atoui, J. Solard, M. Chakaroun, A. Fischer, A. Boudrioua, and L. H. Peng, Post-deposition annealing effect on RF-sputtered TiO_2 thin-film properties for photonic applications, Appl. Phys. A **122** (2016) 78:1−8.

[17] S. Mathur, M. Arya, R. Jain, and S. K. Sharma, Effect of annealing temperature on structural, electrical and optical properties of TiO_2 nanopowder, J. Nanostruct. **7** (2017) 121−126.

[18] R. Kawakami, M. Niibe, Y. Nakano, Y. Araki, Y. Yoshitani, C. Azuma, and T. Mukai,

Characteristics of TiO_2 thin films surfaces treated by O_2 plasma in dielectric barrier discharge with the assistance of external heating, Vacuum **152** (2018) 265−271.

[19] R. Kawakami, Y. Yoshitani, K. Mitani, M. Niibe, Y. Nakano, C. Azuma, and T. Mukai, Effects of air-based nonequilibrium atmospheric pressure plasma jet treatment on characteristics of polypropylene film surfaces, Appl. Surf. Sci. **509** (2020) 144910:1-10.

[20] H. Ohta, F. Horikiri, T. Nakamura, and T. Mishima, Ion-irradiation damage on GaN p-n junction diodes by inductively coupled plasma etching and its recovery by thermal treatment, Nucl. Instr. Meth. Phys. Res. B **409** (2017) 65−68.

[21] A. Hassen, M. Mahrouk, H. Quzari, M. Cherif, A. Boudabous, and J. J. Damelincourt, UV disinfection of treated wastewater in a large-scale pilot plant and inactivation of selected bacteria in a laboratory UV device, Bioresour. Technol. **74** (2000) 141−150.

[22] R. Kawakami, T. Inaoka, S. Minamoto, and Y. Kikuhara, Analysis of GaN etching damage by capacitively coupled RF Ar plasma exposure, Thin Solid Films **516** (2008) 3478−3481.

[23] T. Arlt, M. Bermejo, M.A. Blanco, L. Gerward, J. Z. Jiang, J. S. Olsen, and J. M. Recio, High-pressure polymorphs of anatase TiO_2, Phys. Rev. B **61** (2000) 14414−14419.

[24] R. Kawakami, M. Niibe, A. Takeichi, Y. Mori, M. Konishi, T. Kotaka, F. Matsunaga, T. Takasaki, T. Kitano, T. Miyazaki, T. Inaoka, and K. Tominaga, Characteristics of TiO_2 thin film surfaces treated by helium and air dielectric barrier discharge plasma, Jpn. J. Appl. Phys. **51** (2012) 08HB04:1−6.

[25] R. Kawakami, M. Niibe, Y. Nakano, R. Tanaka, C. Azuma, and T. Mukai, Characteristics of N_2 and O_2 plasma-induced damages on AlGaN thin film surfaces, Phys. Status Solidi A **214** (2017) 1700393:1-7.

[26] U. Cvelbar, N. Krstulovic, S. Milosevic, and M. Mozetie, Inductively coupled RF oxygen plasma characterization by optical emission spectroscopy, Vacuum **82** (2008) 224−227.

[27] J. T. Gudmundsson, I. G. Kouznetsov, K. K. Patel, and M. A. Lieberman, Electronegativity of low-pressure high-density oxygen discharges, J. Phys. D: Appl. Phys. **34** (2001) 1100−1109.

[28] A. Suligoj, U. L. Stangar, A. Ristic, M. Mazaj, D. Verhovsek, and N. N. Tusar, TiO_2−SiO_2 films from organic-free colloidal TiO_2 anatase nanoparticles as photocatalyst for removal of volatile organic compounds from indoor air, Appl. Catal. B: Environ. **184** (2016) 119−131.

[29] L. M. F. Arias, A. A. Duran, D. Cardona, E. Camps, M. E. Gomez, and G. Zambrano, Effect of annealing treatment on the photocatalytic activity of TiO_2 thin films deposited by dc reactive magnetron sputtering, J. Phys. Conf. Ser. **614** (2015) 012008:1−6.

[30] Y. H. Joe, W. Ju, J. H. An, and J. Hwang, A quantitative determination of the antibacterial efficiency of fibrous air filters based on the disc diffusion method, Aerosol Air Qual. Res. **14** (2014) 928−933.

[31] S. Saitoh, K. Iwasaki, and O. Yagi, Development of a most-probable-number method for enumerating denitrifying bacteria by using 96-well microtiter plates and an anaerobic culture system, Microbes Environ. **18** (2003) 210−215.

[32] M. K. Singh, A. Ogino, and M. Nagatsu, Sterilization efficiency of inactivation factors in a microwave plasma device, J. Plasma Fusion Res. Ser. **8** (2009) 560−563.

[33] L. T. T. Nhung, H. Nagata, A. Takahashi, M. Aihara, T. Okamoto, T. Shimohata, K. Mawatari, M. Akutagawa, Y. Kinouchi, and M. Haraguchi, Sterilization effect of UV light on Bacillus spores using TiO_2 films depends on wavelength, J. Med. Invest. **59** (2012) 53−58.

[34] N. R. Mathews, E. R. Morales, M. A. C. Jacome, and J. A. T. Antonio, TiO_2 thin films – Influence of annealing temperature on structural, optical and photocatalytic properties, Sol. Energy **83** (2009) 1499−1508.

[35] H. Berger, H. Tang, and F. Levy, Growth and Raman spectroscopic characterization

of TiO_2 anatase single crystals, J. Cryst. Growth **130** (1993) 108−112.

[36] C. Y. Tsai, Y. T. Pan, Y. H. Tseng, C. W. Liu, T. H. Kuo, and H. C. Hsi, Influence of carbon-functional groups with less hydrophilicity on a TiO_2 photocatalyst for removing low-level elemental mercury, Sust. Environ. Res. **27** (2017) 70−76.

[37] C. Y. Wu, K. J. Tu, J. P. Deng, Y. S. Lo, and C. H. Wu, Markedly enhanced surface hydroxyl groups of TiO_2 nanoparticles with superior water-dispersibility for photocatalysis, Materials **10** (2017) 566:1−15.

[38] R. Kawakami, M. Niibe, T. Fukudome, A. Takeichi, T. Inaoka, and K. Tominaga, Effect of dielectric barrier discharge air plasma treatment on TiO_2 thin film surfaces, Jpn. J. Appl. Phys. **50** (2011) 01BE02:1−5.

[39] P. Bindra and A. Hazra, Impedance behavior of n-type TiO_2 nanotubes porous layer in reducing vapor ambient, Vacuum **152** (2018) 78−83.

[40] J. Lu, K. Liang, C. Xu, X. Wang, H. Ouyang, J. Huang, and L. Feng, Humidity sensor based on heterogeneous $CoTiO_3/TiO_2$ film with vertically aligned nanocrystalline structure, Vacuum **163** (2019) 292−300.

[41] C. Y. Wu, K. J. Tu, J. P. Deng, Y. S. Lo, and C. H. Wu, Markedly enhanced surface hydroxyl groups of TiO_2 nanoparticles with superior water-dispersibility for photocatalysis, Materials **10** (2017) 566: 1−15.

[42] T. Kasuga, H. Kondo, and M. Nogami, Apatite formation on TiO_2 in simulated body fluid, J. Cryst. Growth **235** (2002) 235−240.

[43] R. P. Lynch, A. Ghicov, and P. Schmuki, A photo-electrochemical investigation of self-organized TiO_2 nanotubes, J. Electrochem. Soc. **157** (2010) G76−G84.

[44] Y. Wang and D. J. Doren, First-principles calculations on TiO_2 doped by N, Nd, and vacancy, Solid State Commun. **136** (2005) 186−189.

[45] Y. Chen, X. Luo, Y. Luo, P. Xu, J. He, L. Jiang, J. Li, Z. Yan, and J. Wang, Efficient charge carrier separation in L-alanine acids derived N-TiO_2 nanospheres: the role of

oxygen vacancies in tetrahedral Ti^{4+} Sites, Nanomaterials **9** (2019) 698:1−13.

[46] A. Houas, H. Lachheb, M. Ksibi, E. Elaloui, C. Guillard, and J. M. Herrmann, Photocatalytic degradation pathway of methylene blue in water, Appl. Catal. B Environ. **31** (2001) 145−157.

[47] X. Wang, S.F. Han, Q. W. Zhang, N. Zhang, and D. D. Zhao, Photocatalytic oxidation degradation mechanism study of methylene blue dye waste water with GR/TiO_2, MATEC Web of Conf. **238** (2018) 03006:1−5.

[48] D. Byun, Y. Jin, B. Kim, J. K. Lee, and D. Park, Photocatalytic TiO_2 deposition by chemical vapor deposition, J. Hazard. Mater. B **73** (2000) 199−206.

[49] J. S. Kim and C. W. Ham, Photocatalytic behavior of the coupling of TiO_2-phosphorescent materials using CVD, J. Ceram. Soc. Jpn. **117** (2009) 570−573.

[50] Z. Futera and N. J. English, Exploring rutile (110) and anatase (101) TiO_2 water interfaces by reactive force-field simulation, J. Phys. Chem. C **121** (2017) 6701−6711.

[51] K. Tada, H. Koga, M. Okumura, and S. Tanaka, Clarification of the interaction between Au atoms and the anatase TiO_2 (112) surface using density functional theory, Surf. Sci. **670** (2018) 23−32.

[52] M. L. Sushko and K. M. Rosso, The origin of facet selectivity and alignment in anatase TiO_2 nanoparticles in electrolyte solutions: implications for oriented attachment in metal oxides, Nanoscale **8** (2016) 19714−19725.

[53] T. Berger, M. Sterrer, O. Diwald, E. Knozinger, D. Panayotov, T. L. Tompson, and J. T. Yates, Light-induced charge separation in Anatase TiO_2 Particles, J. Phys. Chem. B. **109** (2005) 6061−6058.

[54] V. S. Becerril, E. Sundin, M. Mapar, and M. Abrahamsson, Extending charge separation life time and distance in patterned dye-sensitized SnO_2−TiO_2 μm-thin films, Phys. Chem. Chem. Phys. **19** (2017) 22684−22690.

[55] PEGASUS Software Inc., http://www.psinc.co.jp/english/products/PHM.html.

[56] PEGASUS Software Inc., http://www.psinc.co.jp/english/products/NMEM.html.

[57] P. Colella, M. R. Dorr, and D. D. Wake, A conservative finite difference method for the numerical solution of plasma fluid equations, J. Comput. Phys. **149** (1999) 168−193.

[58] P. Colella, M. R. Dorr, and D. D. Wake, Numerical solution of plasma fluid equations using locally refined grids, J. Comput. Phys. **152** (1999) 550−583.

[59] W. H. Matthaeus and M. R. Brown, Nearly incompressible magnetohydrodynamics at low Mach number, Phys. Fluids **31** (1988) 3634−3644.

[60] K. Hassouni, S. Cavadias, E. Utku, and J. Amouroux, Use of navier-stokes equations for two dimensional modelling of a low pressure plasma chemical reactor, Comput. Chem. Eng. **17** (1993) S505−S510.

[61] N. Y. Babaeva and M. J. Kushner, Ion energy and angular distributions onto polymer surfaces delivered by dielectric barrier discharge filaments in air: I. flat surfaces, Plasma Sources Sci. Technol. **20** (2011) 035017:1−11.

[62] X. Pan, M. Q. Yang, X. Fu, N. Zhang, and Y. J. Xu, Defective TiO_2 with oxygen vacancies: synthesis, properties and photocatalytic applications, Nanoscale **5** (2013) 3601−3614.

[63] F. Guillemot, M. C. Porte, C. Labrugere, and C. Baquey, Ti^{4+} to Ti^{3+} conversion of TiO_2 uppermost layer by low-temperature vacuum annealing: interest for titanium biomedical applications, J. Colloid. Interf. Sci. **255** (2002) 75−78.

[64] PEGASUS Software Inc., http://www.psinc.co.jp/english/products/SASAMAL.html.

[65] J. P. Biersack and L. G. Haggmark, A Monte Carlo computer program for the transport of energetic ions in amorphous targets, Nucl. Instr. Meth. **174** (1980) 257−269.

[66] J. Gao, J. Lyu, J. Li, J. Shao, Y. Wang, W. Ding, R. Cheng, S. Wang, and Z. He, Localization and stabilization of photogenerated electrons at TiO_2 nanoparticle surface by oxygen at ambient temperature, Langmuir **34** (2018) 7034−7041.

[67] M. Setvin, U. Aschauer, P. Scheiber, Y. F. Li, W. Hou, M. Schmid, A. Selloni, and U.

Diebold, Reaction of O_2 with subsurface oxygen vacancies on TiO_2 anatase (101), Science **341** (2013) 988−991.

[68] L. Sang, Y. Zhang, J. Wang, Y. Zhao, and Y. T. Chen, Correlation of the depletion layer with the Helmholtz layer in the anatase TiO_2-H_2O interface via molecular dynamics simulations, Phys. Chem. Chem. Phys. **18** (2016) 15427−15435.

[69] Z. Zhang and J. T. Yates, Band bending in semiconductors: chemical and physical consequences at surfaces and interfaces, Chem. Rev. **112** (2012) 5520−5551.

[70] A. Furube and S. Hashimoto, Insight into plasmonic hot-electron transfer and plasmon molecular drive: new dimensions in energy conversion and nanofabrication, NPG Asia Mater. **9** (2017) e454:1−24.

[71] X. Huang, H. Li, C. Zhang, S. Tan, Z. Chen, L. Chen, Z. Lu, X. Wang, and M. Xiao, Efficient plasmon-hot electron conversion in Ag–$CsPbBr_3$ hybrid nanocrystals, Nature Commun. **10** (2019) 1163:1−8.

[72] J. Song, X. An, J. Zhou, Y. Liu, W. Wang, X. Li, W. Lan, and E. Xiea, Investigation of enhanced ultraviolet emission from different Ti-capped ZnO structures via surface passivation and surface plasmon coupling, Appl. Phys. Lett. **97** (2010) 122103:1−3.

[73] R. Kawakami, M. Niibe, Y. Nakano, M. Konishi, Y. Mori, H. Takeuchi, T. Shirahama, T. Yamada, and K. Tominaga, Characteristics of TiO_2 surfaces etched by capacitively coupled radio frequency N_2 and He plasmas, J. Phys.: Conf. Ser. **441** (2013) 012038:1−6.

[74] R. Kawakami, K. Tominaga, K. Okada, T. Nouda, T. Inaoka, A. Takeichi, T. Fukudome, and K. Murao, Etch damage characteristics of TiO_2 thin films by capacitively coupled RF Ar plasmas, Vacuum **84** (2010) 1393−1397.

[75] Y. M. Abdulraheem, S. Ghoraishi, L. A. Thai, S. K. Zachariash, and M. Ghannam, The effect of annealing on the structural and optical properties of titanium dioxide films deposited by electron beam assisted PVD, Adv. Mater. Sci. Eng. **2013** (2013) 574738:1−10.

[76] X. Zhao, X. Yi, X. Wang, W. Chu, S. Guo, J. Zhang, B. Liu, and X. Liu, Constructing efficient polyimide(PI)/Ag aerogel photocatalyst by ethanol supercritical drying technique for hydrogen evolution, Appl. Surf. Sci. **502** (2020) 144187:1−8.

[77] Q. Chen, H. Wang, C. Wang, R. Guan, R. Duan, Y. Fang, and X. Hu, Activation of molecular oxygen in selectively photocatalytic organic conversion upon defective TiO_2 nanosheets with boosted separation of charge carriers, Appl. Catal. B Environ. **262** (2020) 118258:1−10.

[78] T. Yoshikawa and Y. Naito, What is oxidative stress?, JMA Journal **45** (2000) 1549−1553.

[79] W. Xu, W. Xie, X. Huang, X. Chen, N. Huang, X. Wang, and J. Liu, The graphene oxide and chitosan biopolymer loads TiO_2 for antibacterial and preservative research, Food Chemistry **221** (2017) 267−277.

[80] O. Akhavan and E. Ghaderi, Toxicity of graphene and graphene oxide nanowalls against bacteria, ACS Nano **4** (2010) 5731−5736.

[81] O. Modesto, P. Hammer, and R. F. P. Nogueira, Gas phase photocatalytic bacteria inactivation using metal modified TiO_2 catalysts, J. Photochem. Photobiol. A: Chem. **253** (2013) 38−44.

[82] H. M. Yadav, S. V. Otari, R. A. Bohara, S. S. Mali, S. H. Pawar, and S. D. Delekar, Synthesis and visible light photocatalytic antibacterial activity of nickel-doped TiO_2 nanoparticles against Gram-positive and Gram-negative bacteria, J. Photochem. Photobiol. A: Chem. **294** (2014) 130−136.

Figure captions:

Fig. 1. (a) Photograph of anatase TiO_2 NPs immobilized on glass substrate. Photograph comparing (b) anatase TiO_2 NPs-immobilized and (c) anatase TiO_2 NPs-incompletely-immobilized samples when immersed in deionized water.

Fig. 2. (a) Photographs of setup before discharge and NAP O_2 plasma discharge with external heating. (b) Waveforms of applied voltage and discharge current for NAP O_2 plasma discharge with external heating.

Fig. 3. (a) MB dye photodecomposition values, $|\ln(C/C_0)|$, of untreated and plasma-assisted-annealed TiO_2 NPs. (b) MB dye photodecompositions, $|\ln(C/C_0)|$, of TiO_2 NPs annealed at a variety of temperatures by an EF.

Fig. 4. Bacterial inactivation effects of untreated, plasma-assisted-annealed, and 400 ℃ EF-annealed TiO_2 NPs in the presence and absence of an irradiation for 30 s with 3.4 eV photon irradiation.

Fig. 5. XRD patterns of untreated, plasma-assisted-annealed, and 400 ℃ EF-annealed TiO_2 NPs immobilized on glass substrate.

Fig. 6. Ti 2p regions in XPS spectra of untreated, plasma-assisted-annealed, and 400 ℃ EF-annealed TiO_2 NPs.

Fig. 7. O 1s regions in XPS spectra of (a) untreated TiO_2 NPs, (b) plasma-assisted-annealed TiO_2 NPs, and (c) 400 ℃ EF-annealed TiO_2 NPs.

Fig. 8. O/Ti ratios of (a) O−Ti bond, (b) bridging O groups, and (c) terminal O groups for untreated, plasma-assisted-annealed, and 400 ℃ EF-annealed TiO_2 NPs.

Fig. 9. UV absorption coefficients of untreated, plasma-assisted-annealed, and 400 ℃ EF-annealed TiO_2 NPs at a photon energy of 3.4 eV.

Fig. 10. (a) Electrical conductivities of untreated, plasma-assisted-annealed, and 400 ℃ EF-annealed TiO_2 NPs in the presence and absence of 3.4 eV photon irradiation. (b) UV-induced relative electrical conductivities of the samples.

Fig. 11. SEM images of the surfaces of untreated, plasma-assisted-annealed, and 400 ℃ EF-annealed TiO_2 NPs immobilized on glass substrate. The red arrows are indicative of TiO_2 NP agglomerates with large sizes more than 50 μm.

Fig. 12. (112)/(101) plane intensity ratios of untreated, plasma-assisted-annealed, and 400 ℃ EF-annealed TiO_2 NPs.

Fig. 13. Calculated fluences of oxygen-based species coming from NAP O_2 plasma onto the sample surface.

Fig. 14. Calculated depth profiles of oxygen vacancies introduced in TiO_2 NPs via the impact of oxygen ions coming from NAP O_2 plasma.

Fig. 15. Nyquist plots of untreated, plasma-assisted-annealed, and 400 ℃ EF-annealed TiO_2 NPs immobilized on glass substrate.

Fig. 16. Proposed enhancement mechanism of photodecomposition of anatase TiO_2 NPs annealed with the assistance of NAP O_2 plasma. Structural models of (112) and (101) anatase TiO_2 surfaces are referenced from literature [52].

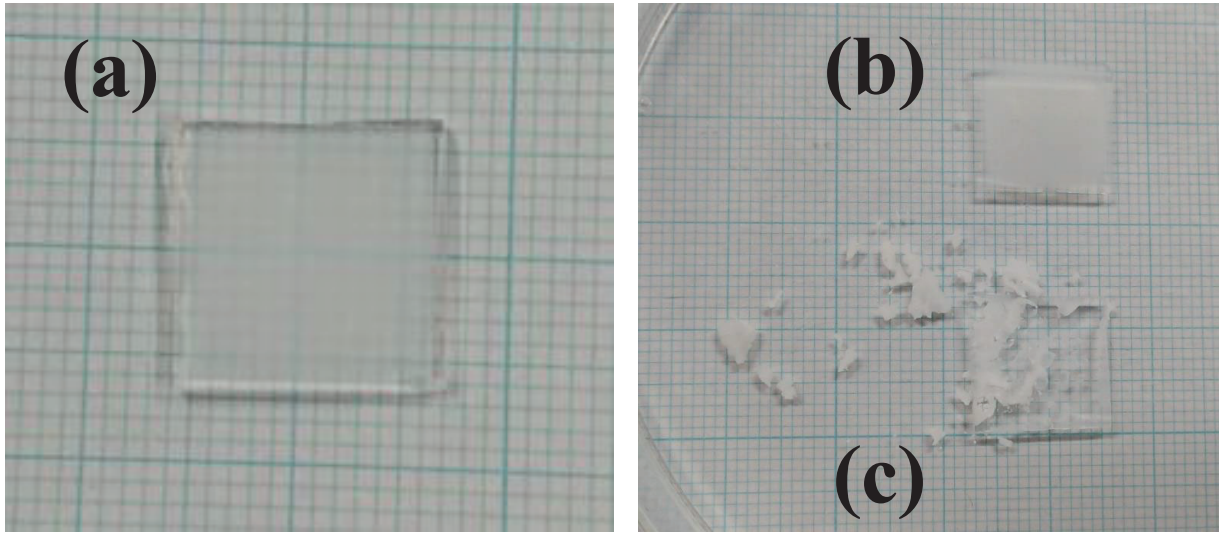

Fig. 1. R. Kawakami *et al*.

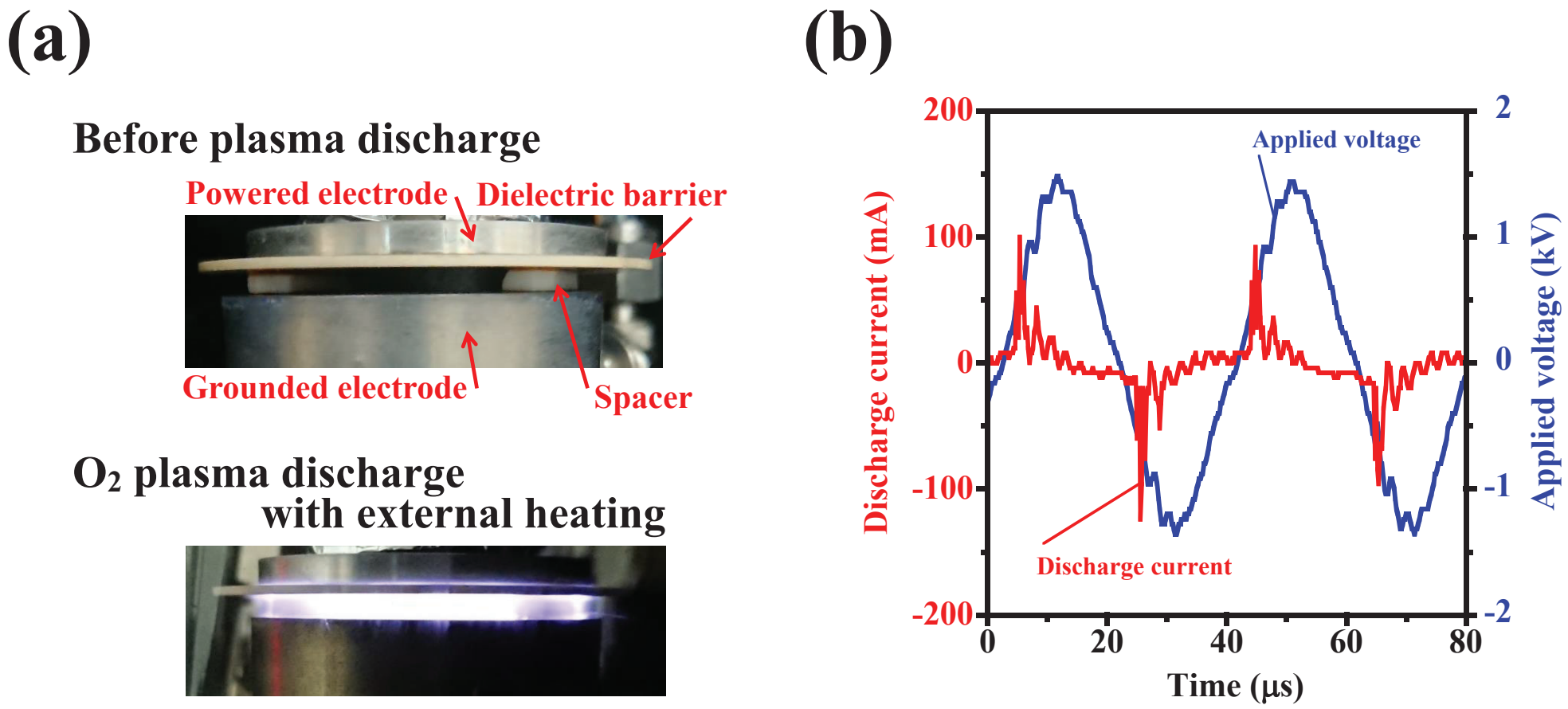

Fig. 2. R. Kawakami *et al.*

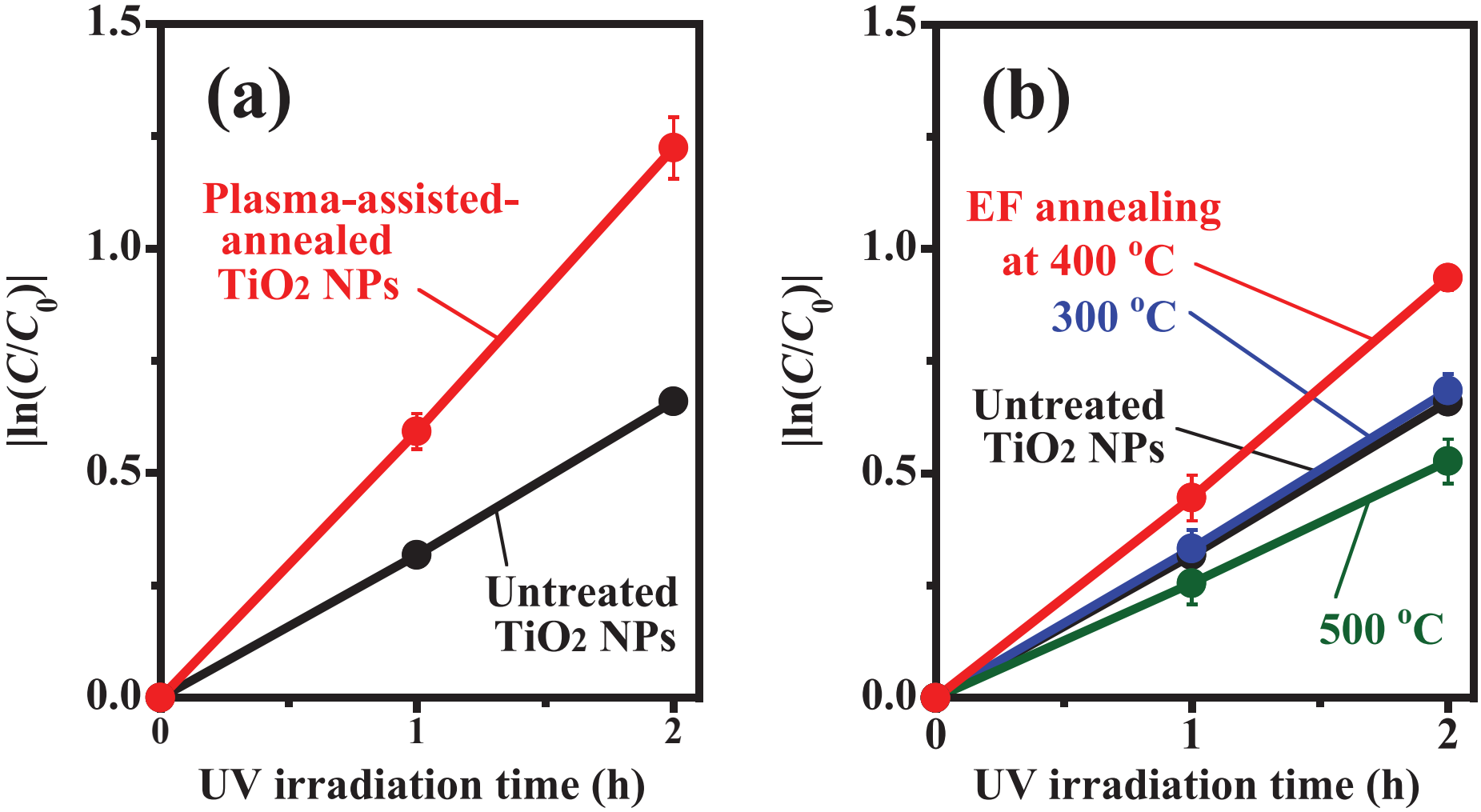

Fig. 3. R. Kawakami *et al.*

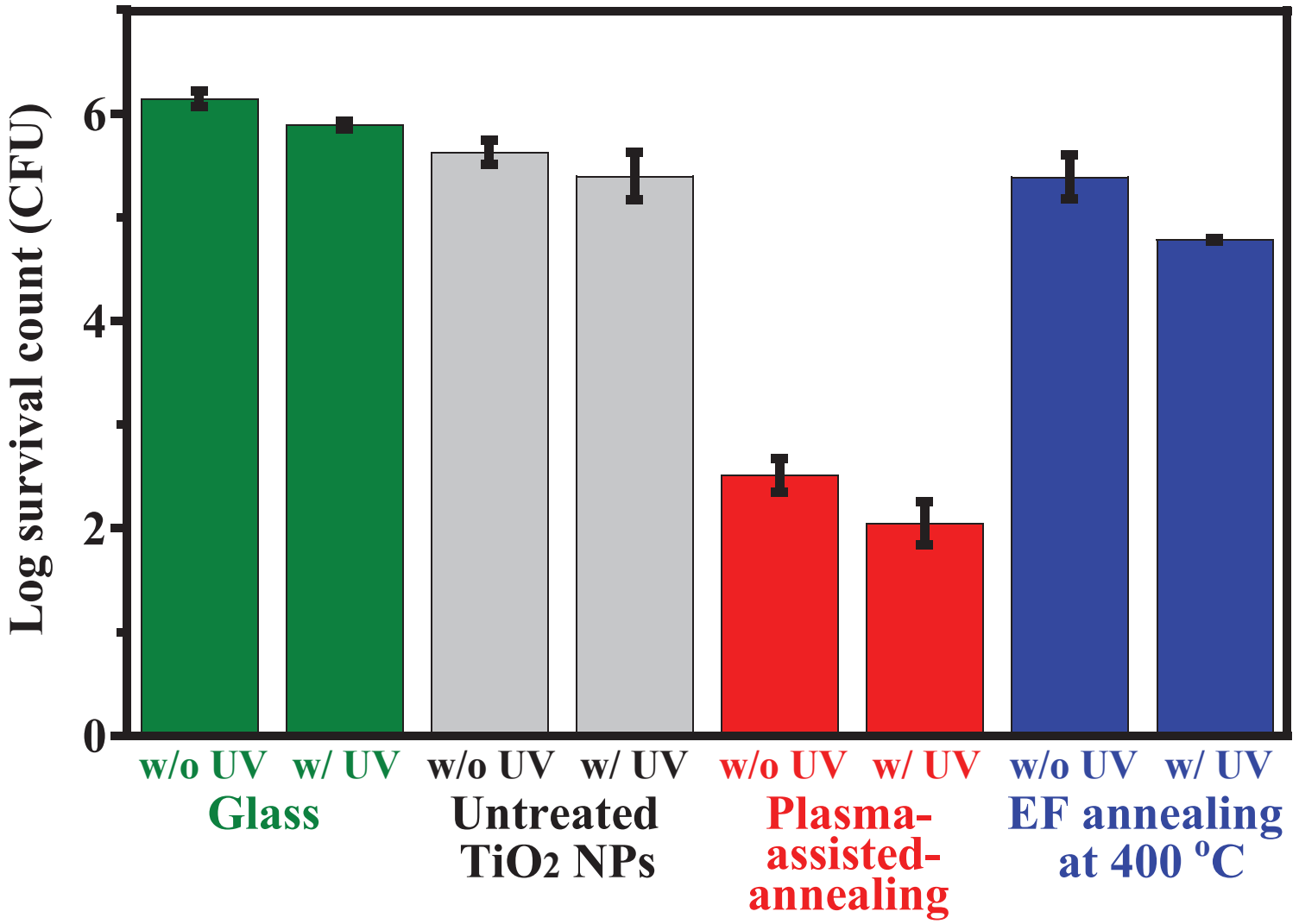

Fig. 4. R. Kawakami *et al.*

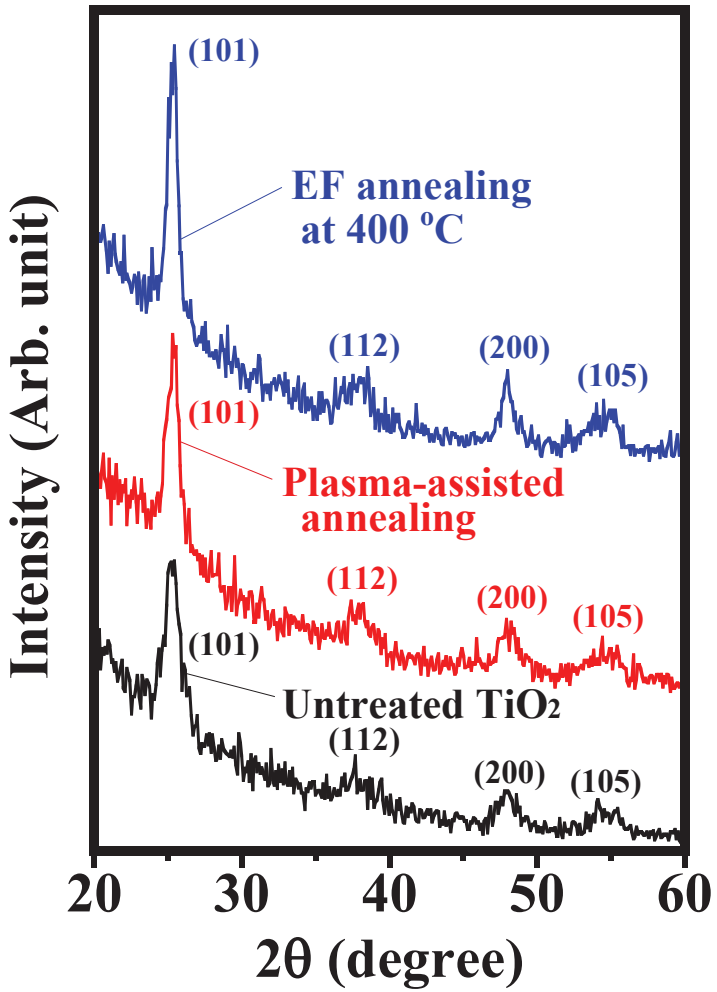

Fig. 5. R. Kawakami *et al*.

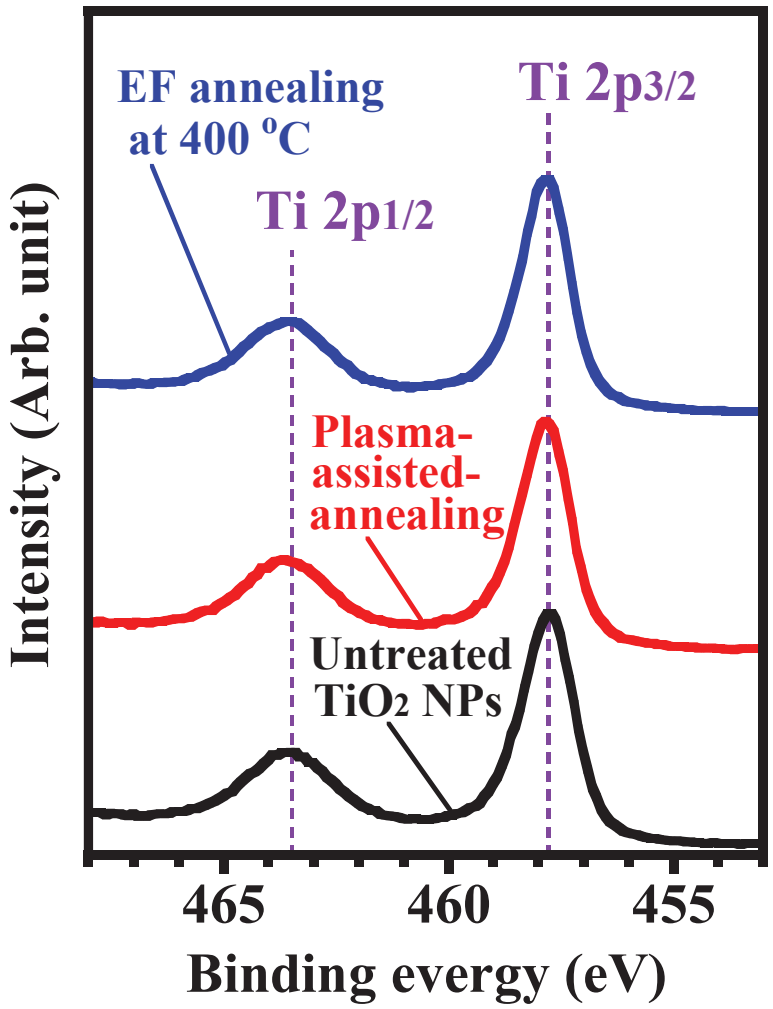

Fig. 6. R. Kawakami *et al.*

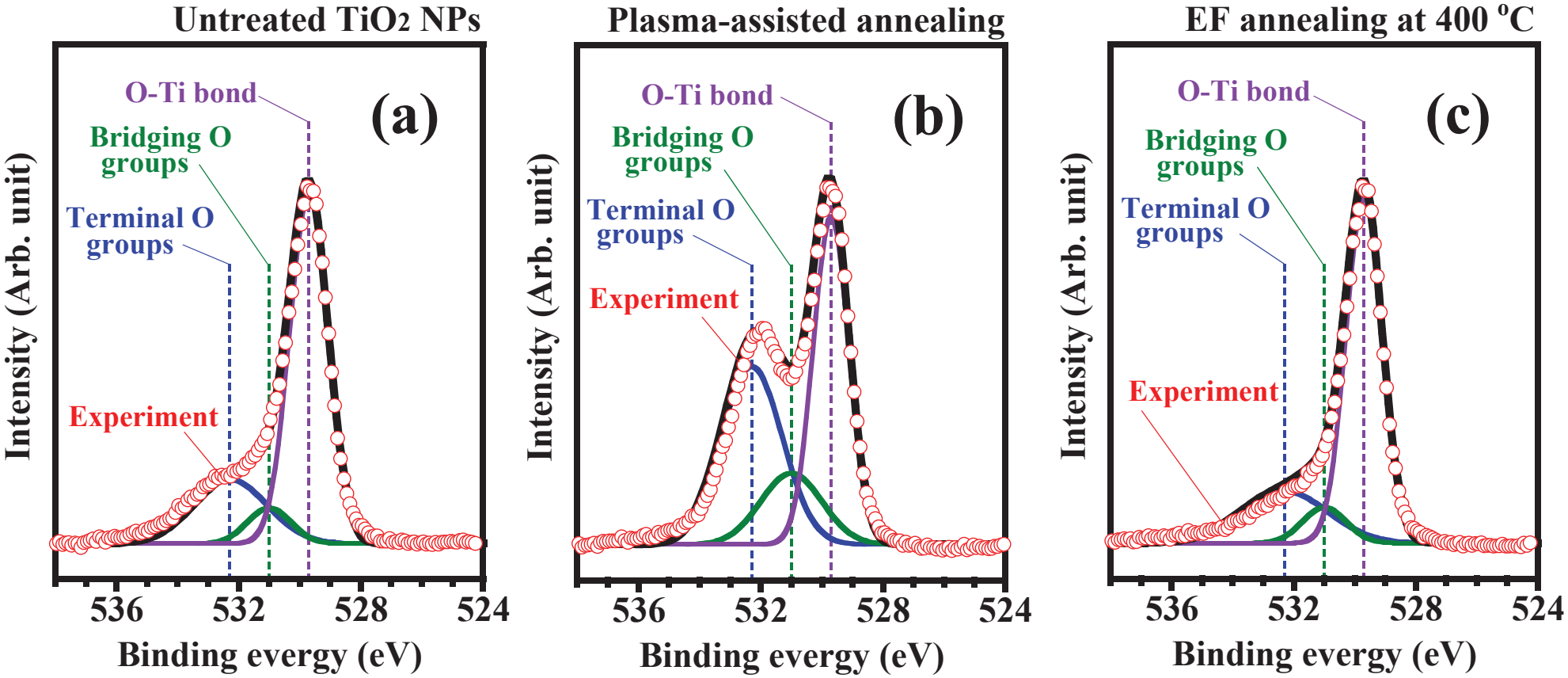

Fig. 7. R. Kawakami *et al.*

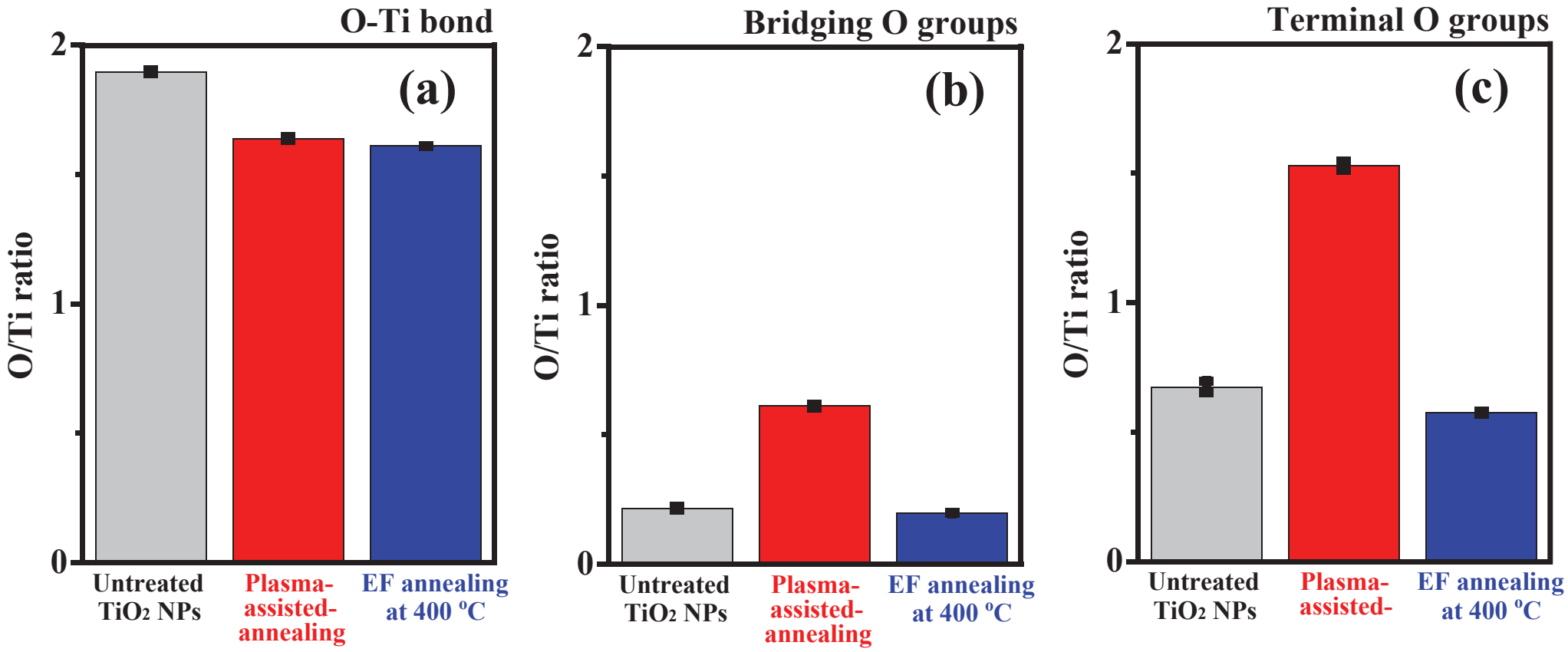

Fig. 8. R. Kawakami *et al.*

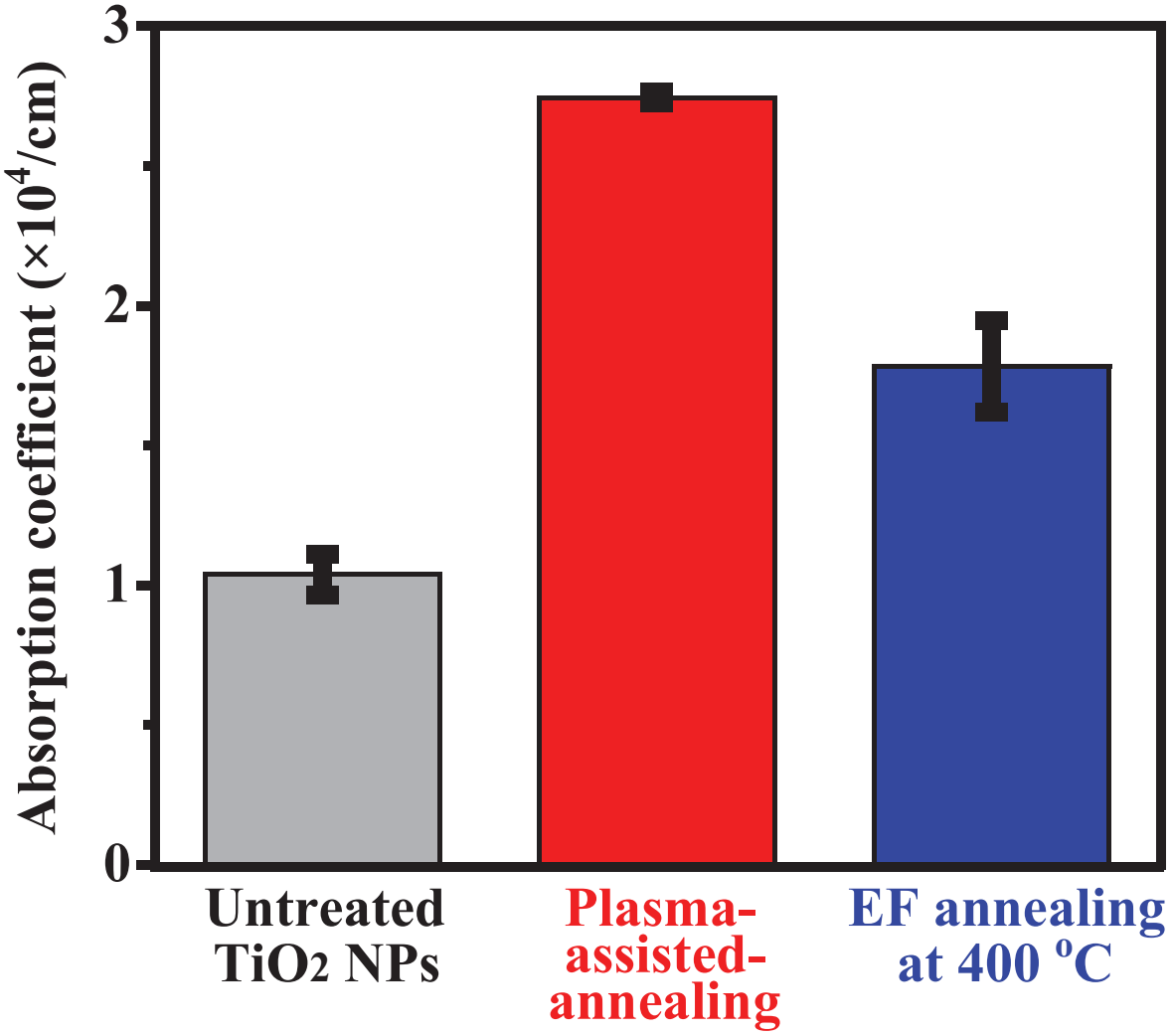

Fig. 9. R. Kawakami *et al.*

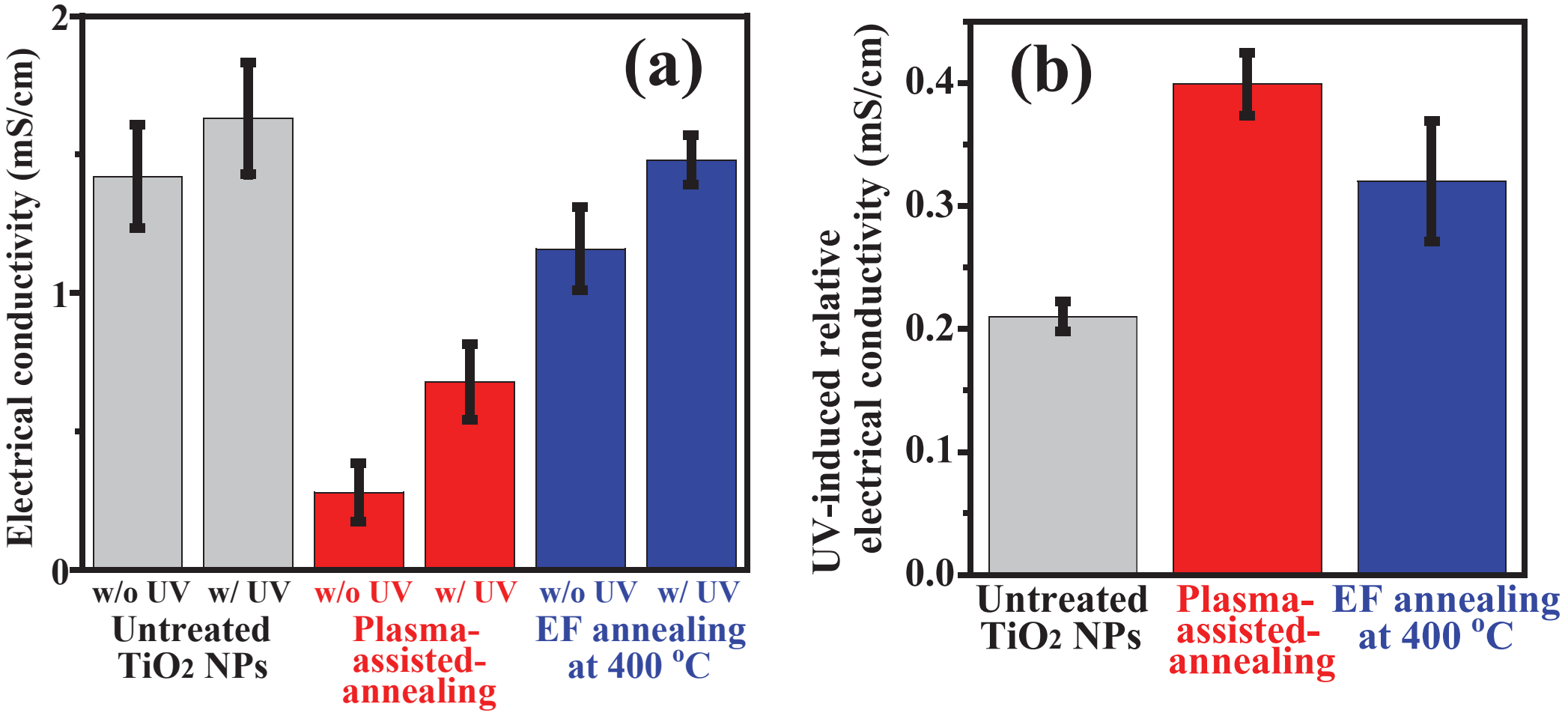

Fig. 10. R. Kawakami *et al.*

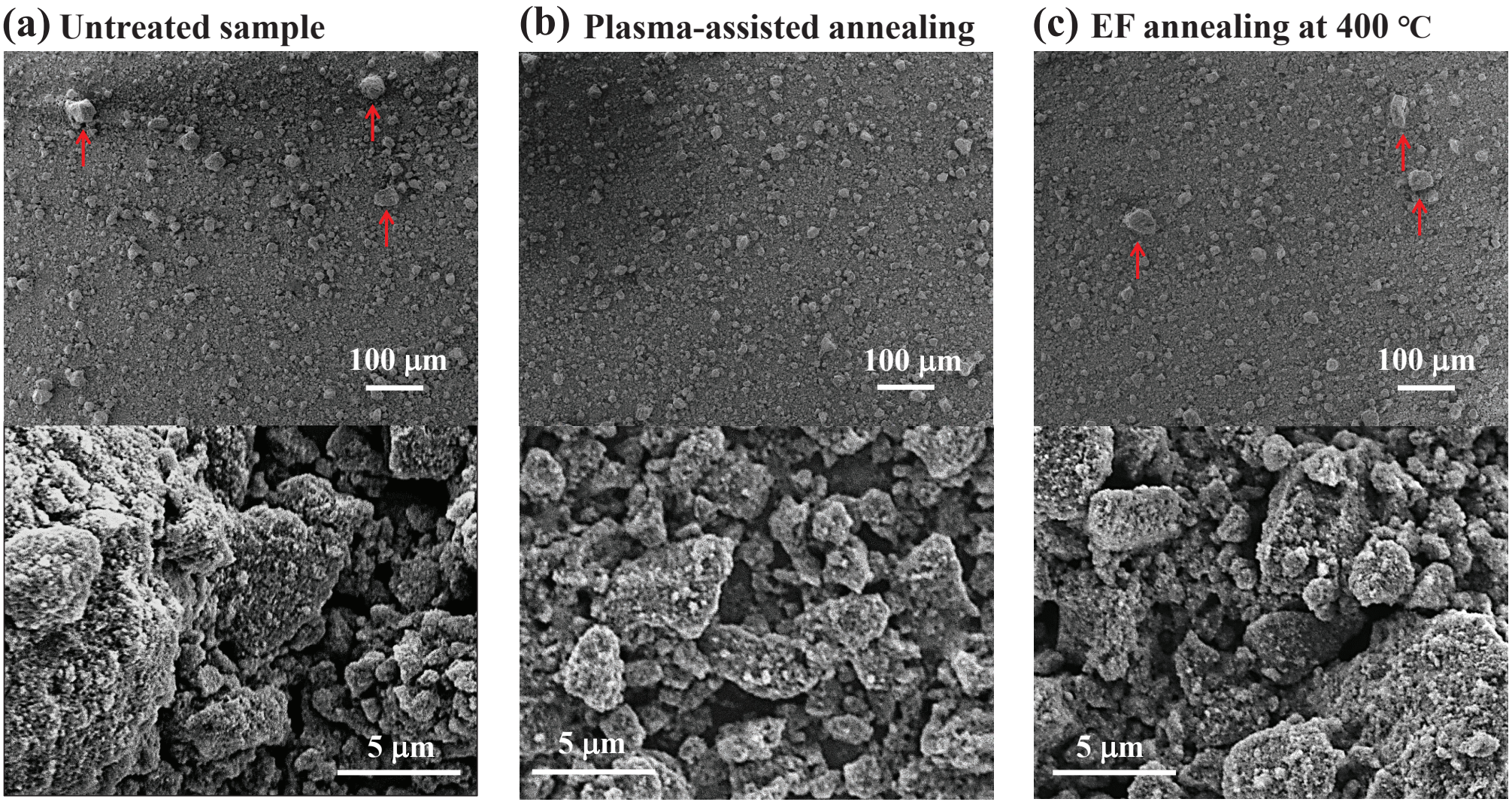

Fig. 11. R. Kawakami *et al*.

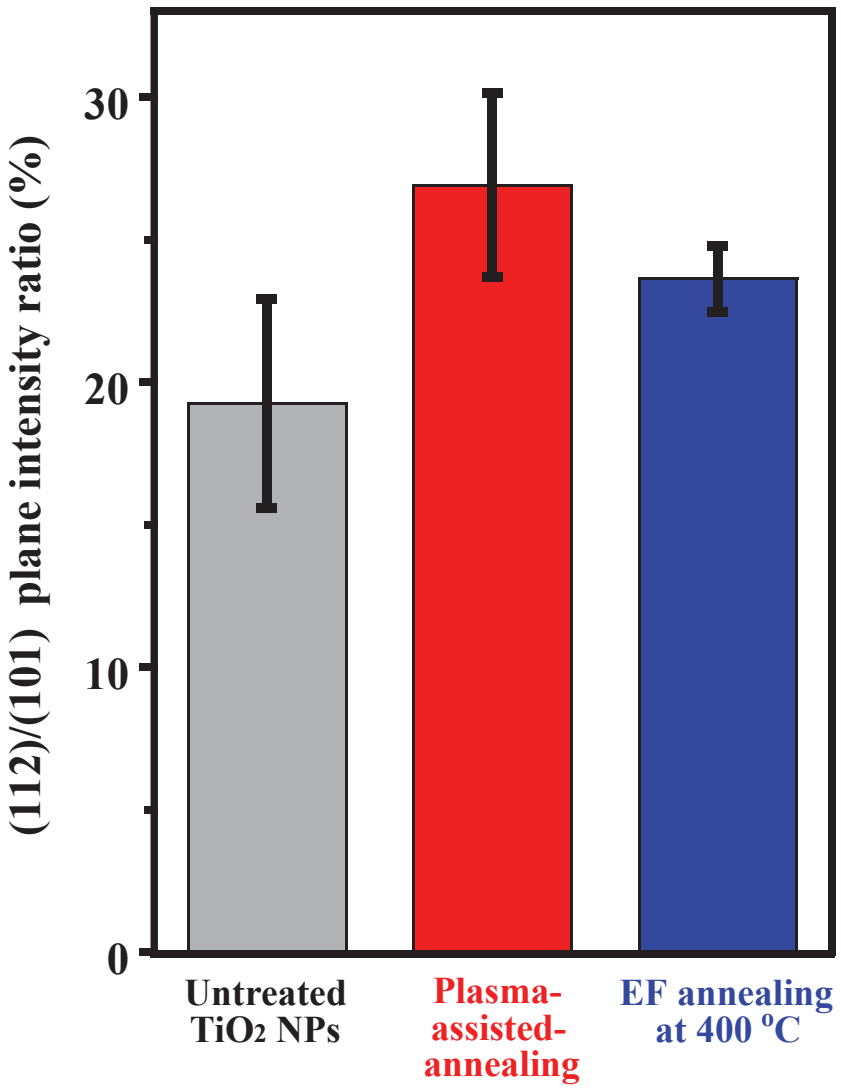

Fig. 12. R. Kawakami *et al.*

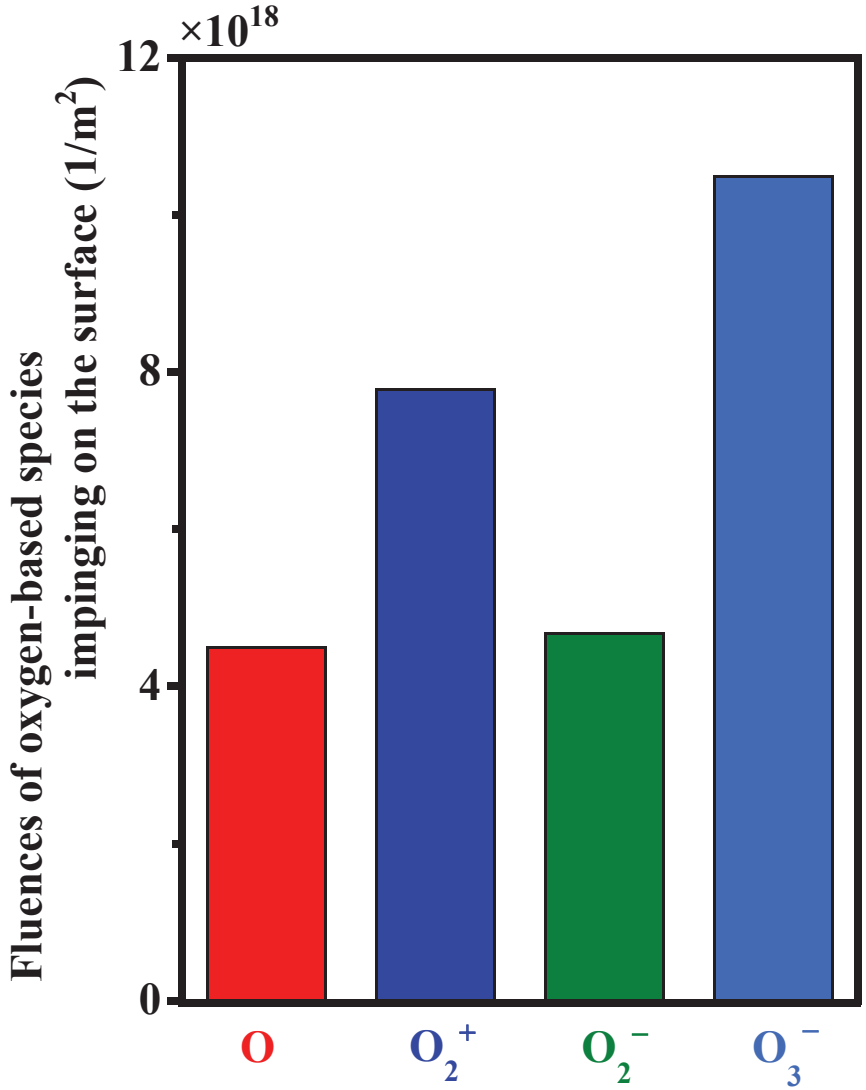

Fig. 13. R. Kawakami *et al.*

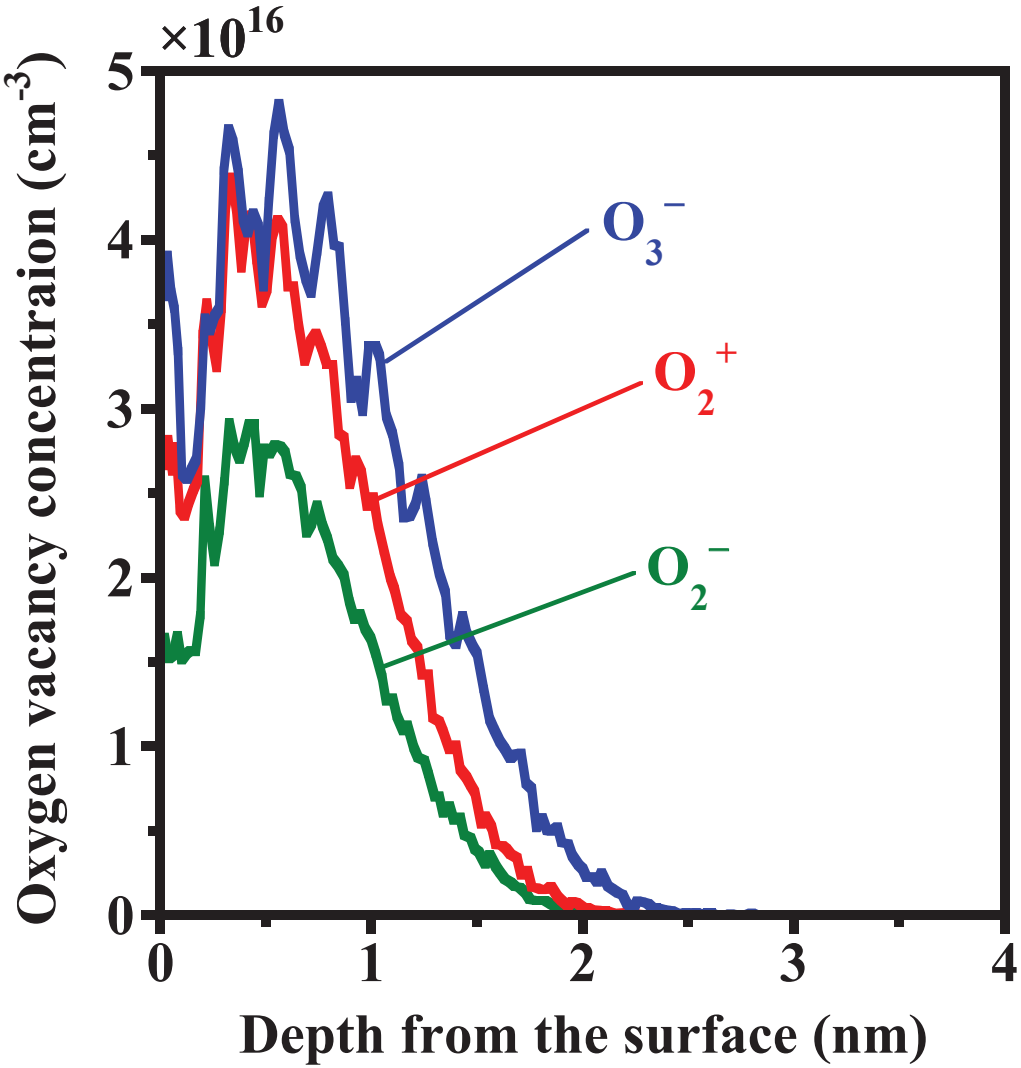

Fig. 14. R. Kawakami *et al.*

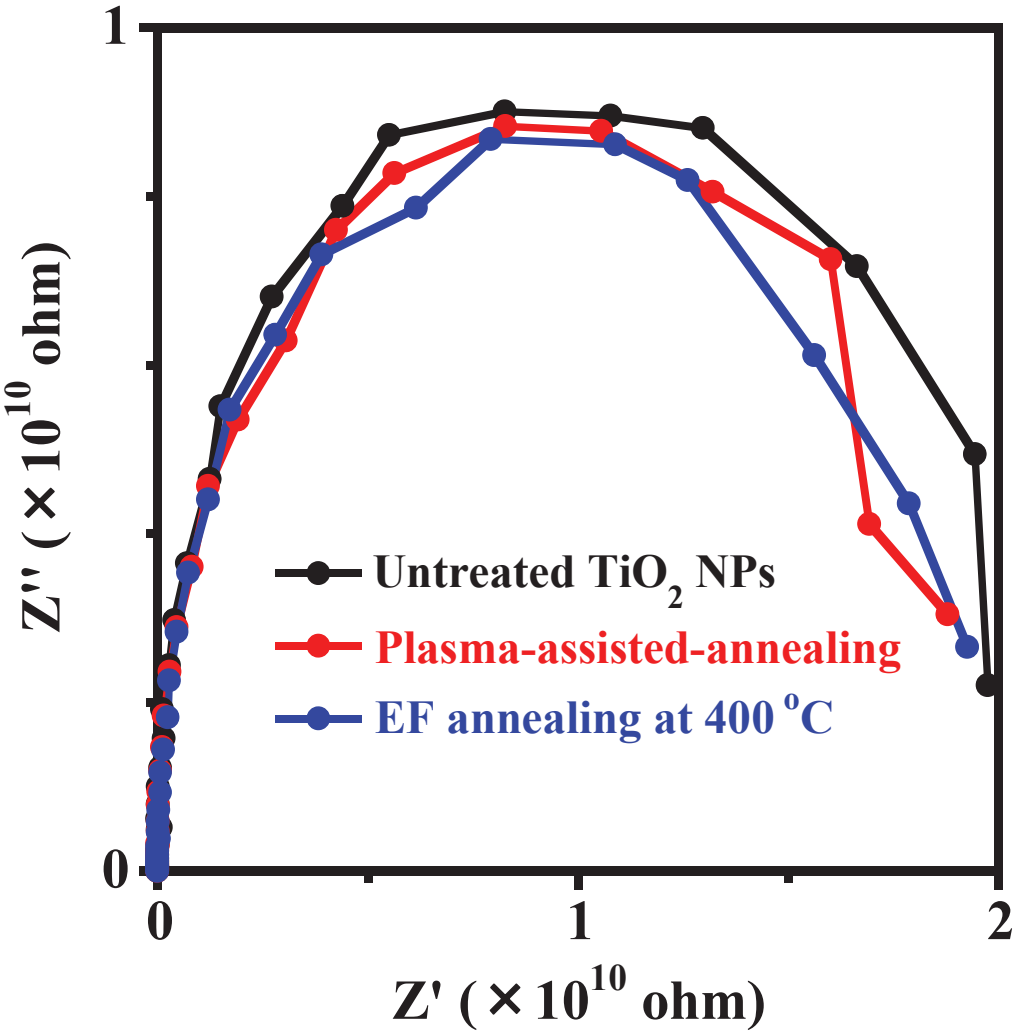

Fig. 15. R. Kawakami *et al.*

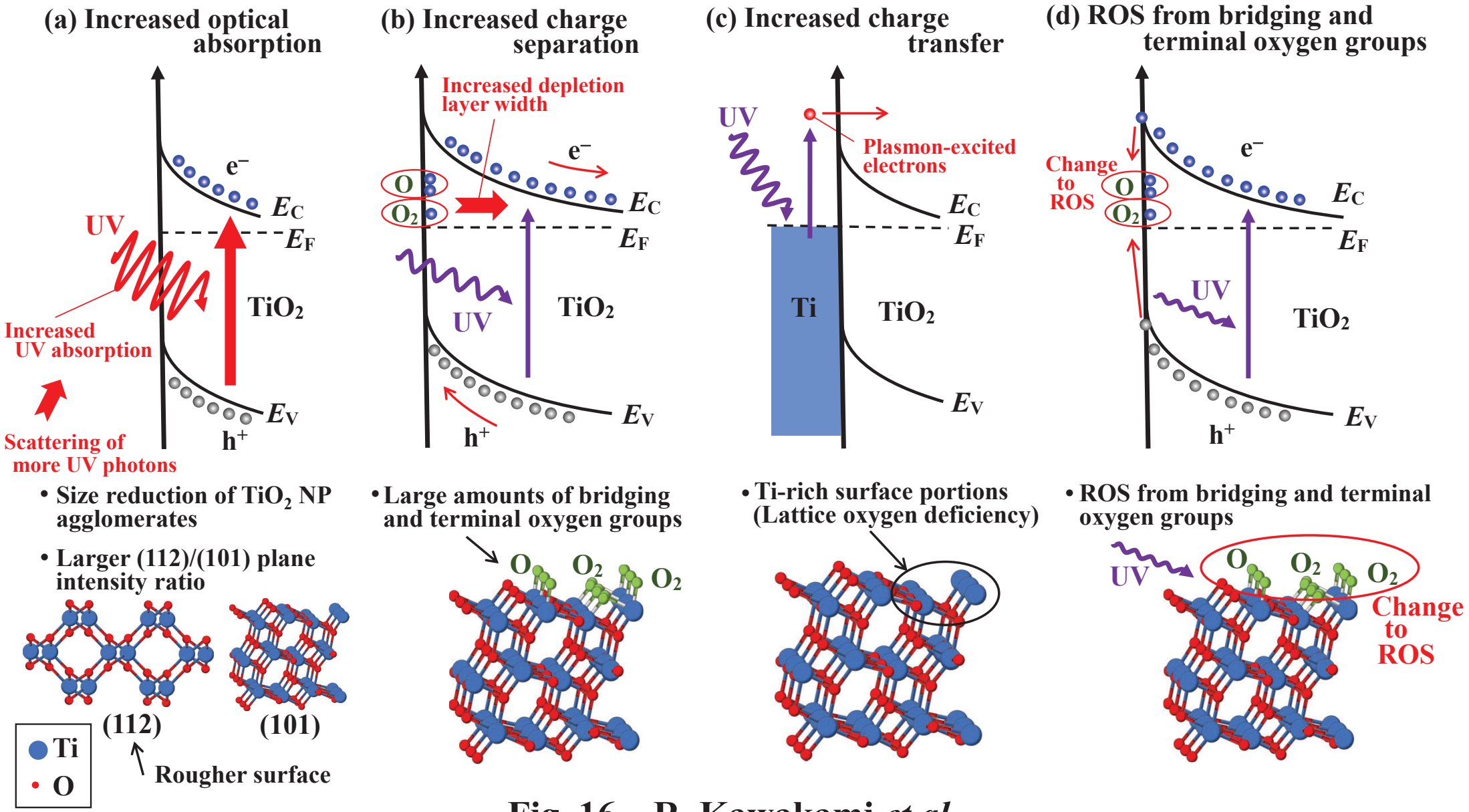

Fig. 16. R. Kawakami *et al.*